Supplementary Information

Secondary nucleation guided noncovalent synthesis of dendritic homochiral superstructures via growth on and from surface

Sai Rachana Pramatha[1], Dasari Srideep[1], Udaijit Pattnaik[2], Rahul Sahu[3], Devamrutha Ilayidathu Suresh[2], Aditya Chandrakant Yadav[1,4], Chinmayee Muduli[5], Sandeep K. Reddy[3], Satyaprasad P. Senanayak[2]*& Kotagiri Venkata Rao[1]*

[1]Department of Chemistry, Indian Institute of Technology Hyderabad, Kandi, Sangareddy, Telangana 502285, India.

[2]Nanoelectronics and Device Physics Lab, School of Physical Sciences, National Institute of Science Education and Research (NISER), Bhubaneswar, OCC of HBNI, Jatni, Khurdha, Odisha 752050, India.

[3]Centre for Computational and Data Science, Indian Institute of Technology Kharagpur, Kharagpur, West Bengal 721302, India.

[4]Department of Materials Science and Metallurgical Engineering, Indian Institute of Technology Hyderabad, Kandi, Sangareddy, Telangana-502284, India.

[5]ICAR-Central Institute of Freshwater Aquaculture, Bhubaneswar, 751002, India.

*Corresponding authors: kvrao@chy.iith.ac.in and satyaprasad@niser.ac.in

Table of contents

1. Supplementary notes

Supplementary Note 1: General

All reagents were bought from TCI or Sigma Aldrich or SRL and used as received unless specified. ^{1}H and ^{13}C NMR spectra were recorded on Bruker 400 MHz and 150 MHz spectrometers at 295 K, respectively, where chemical shifts (δ in ppm) were determined by fixing the solvent peak position. MALDI was performed on Bruker daltonics Autoflex Speed MALDI TOF System (GT0263G201) spectrometer using matrix of trans-2-[3-(4-tert-Butylphenyl)-2-methyl-2-propenylidene] malononitrile (DCTB). FT-IR spectra were recorded using a JASCO model FTIR-4600. Melting points were measured in capillary tubes using the Tempo and Mettler FP1 melting point instrument. Electronic absorption spectra were recorded using a JASCO model V-770 UV-VIS-NIR spectrophotometer in a screw-capped quartz cell of 10 mm or 1 mm optical path length. Fluorescence spectra were recorded using a JASCO model FP-8300 spectrometer in a screw-capped quartz cell of 10 mm optical path length. Circular dichroism was performed on JASCO J-815 spectropolarimeter. Linear dichroism measurements were performed on JASCO 1600 CD spectrophotometer. DLS was performed using Anton paar litesizer 500. AFM was performed using Park systems NX 10 AFM, in non-contact mode (NCM). NSG 30 tip was used which has a force constant of 96 KHz. Typical scan rates of 0.3 Hz were used. Field Emission Scanning Electron Microscopy (FE-SEM) measurements were performed on a JEOL JIB4700F (FIB-SEM) before the measurement; all samples were spin-coated on the silicon substrate and dried under air followed by evaporation of solvent under vacuum at room temperature. TEM measurements were done on JEOL JEM COLD-FEG F200 where the sample was deposited on a 300 mesh copper grid with lacey carbon support. Thermogravimetric analysis (TGA) was carried out on TA instrument SDT Q 600 using alumina crucible under nitrogen gas flow rate of 100 mL min^{-1} and a heating rate of 10 °C min^{-1}. To electrically monitor the aggregation we performed detailed I-V characterization in the solution phase and dynamically monitored the temporal change in conductivity upon aggregation. Furthermore, the chiro-optical response of the supramolecular assembly was monitored in solution phase upon illumination of appropriate (left circularly and/or right circularly) polarized light and measuring the variation in photocurrent with time after the formation of DHS structures.

Supplementary Note 2: Synthesis and Characterisation

Synthesis and characterisation of ***A*-PDI**[1], ***S*-PDI**[1] and ***R*-PDI**[2] have already been reported by our group and are also described below. (S) and (R)-2-aminoheptane were purchased from Alfa Aesar. Racemic 2-aminoheptane and 4-Phenyl-1,2,4-triazolin-3,5-dione was purchased from TCI Chemicals.

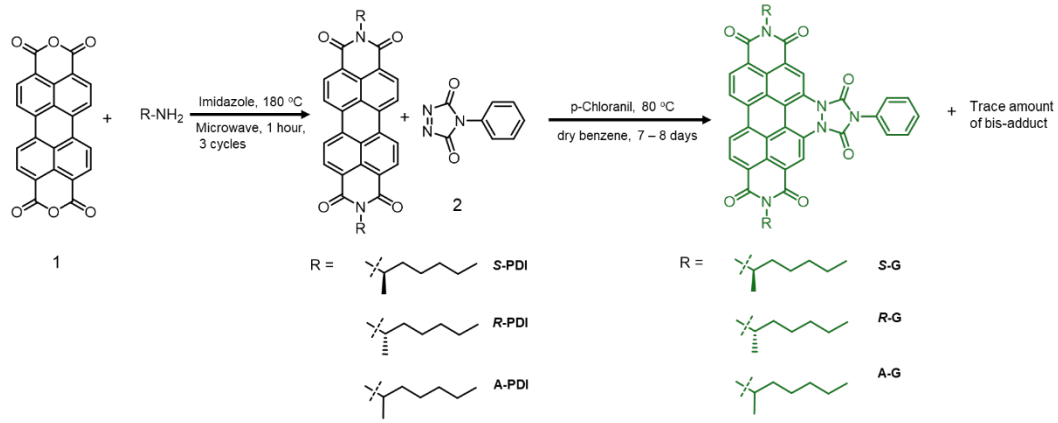

Supplementary Figure 1. Synthesis scheme. General reaction scheme for the synthesis of NIR triimides (***S*-G**, ***R*-G** and ***A*-G**).

Synthesis and characterisation of *S*-PDI-

PTCDA (1) (600 mg, 1 equivalent, 1.53 mmol) was taken in a pressure tight 30 mL microwave vial. To this, imidazole (6 gm) was added and heated to melt imidazole. The mixture was purged with nitrogen gas for 30 minutes. To this reaction mixture, (S)-(+)-2-aminoheptane (1.148 mL, 880mg, 5 equivalents, 7.65mmol) was added under inert conditions. The reaction mixture was subjected to microwave irradiation at 180 ^{o}C for 1 hour and later cooled down. This was done for 3 cycles, each of 1 hour. The obtained dark red solution was washed with 50 mL of 3 M HCl and methanol to remove imidazole. The precipitate was washed multiple times with methanol then vacuum dried to obtain pure product ***S*-PDI**. Yield: 93.7% (840 mg). ^{1}H NMR (400 MHz, $CDCl_3$) δ 8.64 (d, J = 8.0 Hz, 4H), 8.57 (d, J = 8.1 Hz, 4H), 5.29 (m, 2H), 2.26 – 2.14 (m, 2H), 1.94 (m, 2H), 1.62 (d, J = 6.9 Hz, 6H), 1.30 (m, 12H), 0.85 (t, J = 7.0 Hz, 6H).

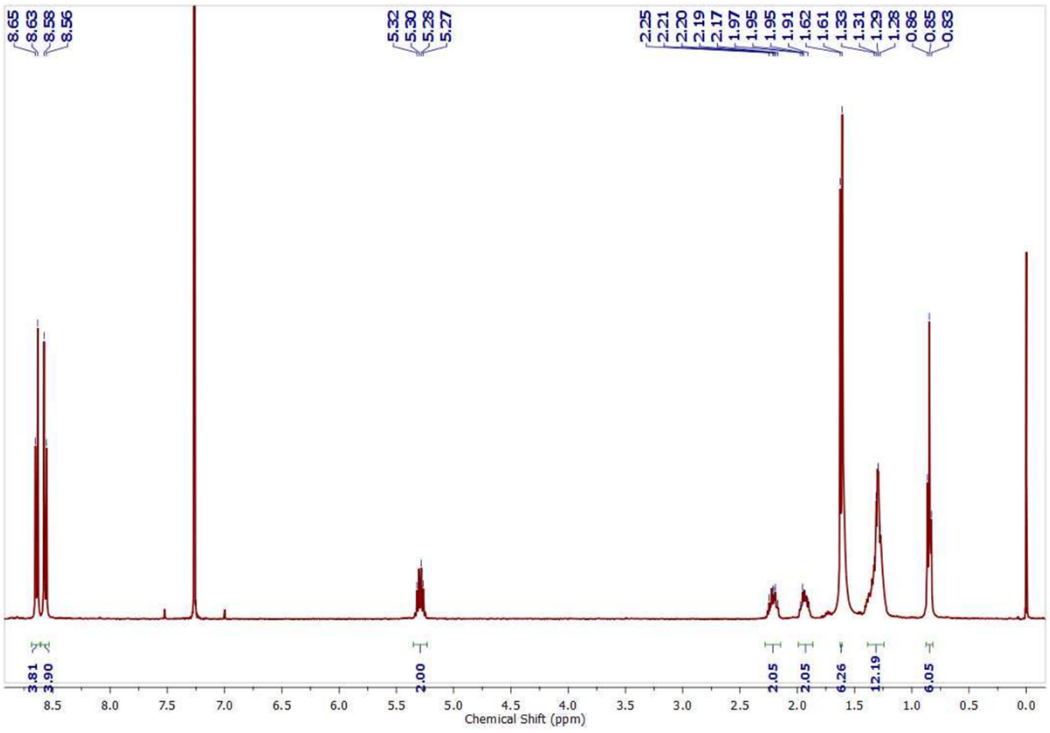

Supplementary Figure 2. ^{1}H-NMR characterisation. ^{1}H-NMR spectrum (400 MHz) of ***S*-PDI** in $CDCl_3$ (concentration: 3 mg in 0.5mL of $CDCl_3$).

Synthesis and characterisation of *R*-PDI-

PTCDA (1) (500 mg, 1 equivalent, 1.27 mmol) was taken in a pressure tight 30 mL microwave vial. To this, imidazole (5 gm) was added and heated to melt imidazole. The mixture was purged with nitrogen gas for 30 minutes. To this reaction mixture, (R)-(+)-2-aminoheptane (0.96 mL, 730 mg, 5 equivalents, 6.377 mmol) was added under inert conditions. The reaction mixture was subjected to microwave irradiation at 180 ^{o}C for 1 hour and later cooled down. This was done for 3 cycles, each of 1 hour. The obtained dark red solution was washed with 50 mL of 3 M HCl and methanol to remove imidazole. The precipitate was washed multiple times with methanol then vacuum dried to obtain pure product ***R*-PDI**. Yield: 95% (710 mg). ^{1}H NMR (400 MHz, $CDCl_3$) δ 8.63 (d, J = 8.0 Hz, 4H), 8.55 (d, J = 8.1 Hz, 4H), 5.29 (m, 2H), 2.21 (m, 2H), 2.00 – 1.87 (m, 2H), 1.62 (d, J = 6.9 Hz, 6H), 1.42 – 1.24 (m, 12H), 0.85 (t, J = 7.0 Hz, 6H).

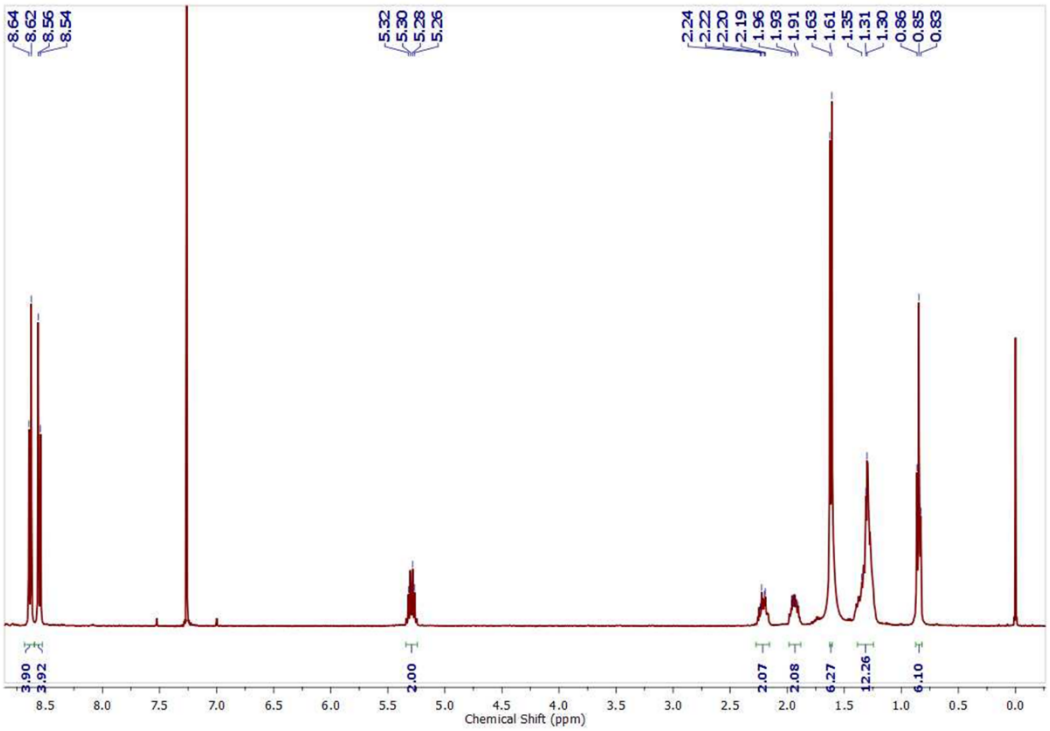

Supplementary Figure 3. ^{1}H-NMR characterisation. ^{1}H-NMR spectrum (400 MHz) of ***R*-PDI** in $CDCl_3$ (concentration: 3 mg in 0.5mL of $CDCl_3$).

Synthesis and characterisation of *A*-PDI-

PTCDA (1) (400 mg, 1 equivalent, 1.02 mmol) was taken in a pressure tight 30 mL microwave vial. To this, imidazole (4 gm) was added and heated to melt imidazole. The mixture was purged with nitrogen gas for 30 minutes. To this reaction mixture, 2-aminoheptane (0.768 mL, 584 mg, 5 equivalents, 5.1 mmol) was added under inert conditions. The reaction mixture was subjected to microwave irradiation at 180 ^{o}C for 1 hour and later cooled down. This was done for 3 cycles, each of 1 hour. The obtained dark red solution was washed with 50 mL of 3 M HCl and methanol to remove imidazole. The precipitate was washed multiple times with methanol then vacuum dried to obtain pure product ***A*-PDI**. Yield: 92% (550 mg). ^{1}H NMR (400 MHz, $CDCl_3$) δ 8.65 (d, J = 8.0 Hz, 4H), 8.58 (d, J = 8.1 Hz, 4H), 5.35 – 5.24 (m, 2H), 2.22 (m, 2H), 1.98 – 1.85 (m, 2H), 1.61 (d, J = 6.9 Hz, 6H), 1.40 – 1.23 (m, 12H), 0.85 (t, J = 7.0 Hz, 6H).

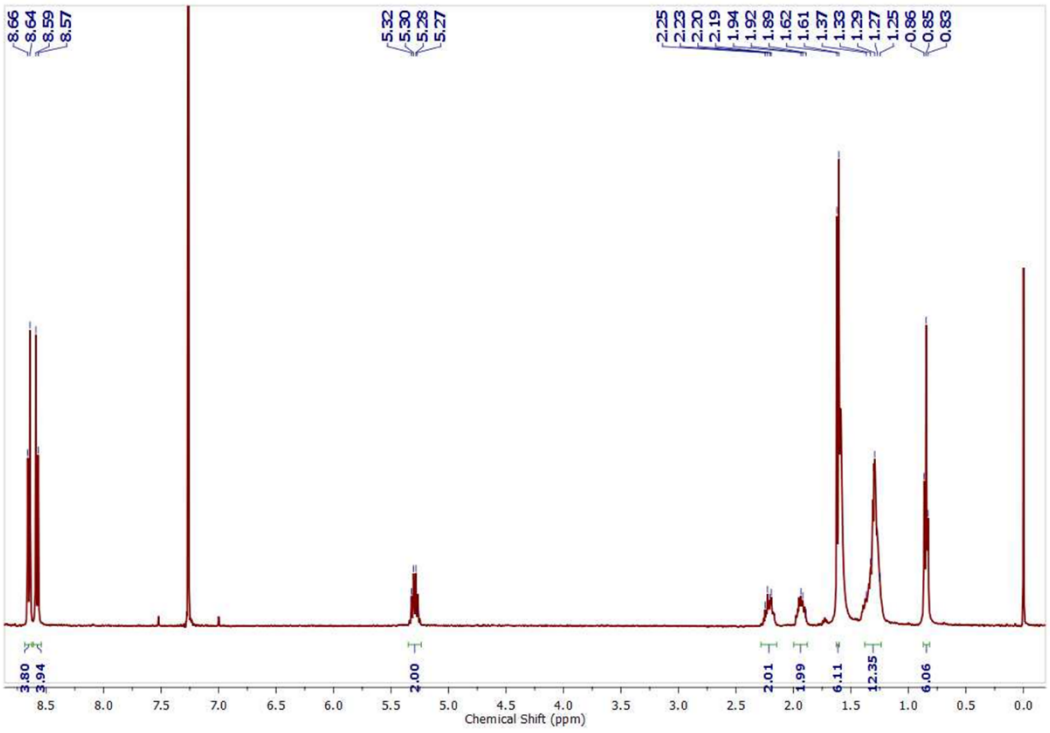

Supplementary Figure 4. ^{1}H-NMR characterisation. ^{1}H-NMR spectrum (400 MHz) of ***A*-PDI** in $CDCl_3$ (concentration: 3 mg in 0.5mL of $CDCl_3$).

Synthesis and characterisation of *S*-G

In a 25 mL double-necked round bottom flask, ***S*-PDI**[1] (150 mg, 1 equivalent, 0.255 mmol) was taken. To this**, 4-Phenyl-1,2,4-triazolin-3,5-dione** (2) (223 mg, 5 equivalents, 1.278 mmol) and p-Chloranil (251 mg, 4 equivalents, 1.022 mmol) were added. The round bottom flask was then charged with anhydrous benzene (10 mL). This reaction mixture was degassed by bubbling with nitrogen gas for over 30 min. This reaction mixture was refluxed at 80 ºC for a period of 7 days. The reaction mixture turned green. The reaction mixture was allowed to cool to room temperature to give precipitate, after which it was washed with hexane and acetone to yield a green coloured solid upon drying under reduced pressure[3]. Further purification of this was done by column chromatography on silica gel. The eluant used was 98:2 Chloroform: Acetone to afford the final green product, ***S*-G**. Yield: 50% (97 mg). ^{1}H NMR (400 MHz, $CDCl_3$) δ 9.14 (s, 2H), 8.25 (d, J = 7.9 Hz, 2H), 8.02 (d, J = 8.1 Hz, 2H), 7.77 – 7.68 (m, 2H), 7.65 – 7.50 (m, 3H), 5.26 – 5.05 (m, 2H), 2.13 (d, J = 18.3 Hz, 2H), 1.92 (d, J = 13.3 Hz, 2H), 1.60 (d, J = 6.9 Hz, 6H), 1.31 (t, J = 19.4 Hz, 12H), 0.85 (t, J = 7.0 Hz, 6H). ^{13}C NMR (150 MHz, $CDCl_3$) δ 162.29, 161.62, 142.93, 132.89, 132.20, 129.82, 129.43, 129.25, 126.19, 125.82, 124.58, 123.32, 117.69, 116.24, 50.55, 33.37, 31.65, 26.83, 22.59, 17.86, 14.09. IR (KBr) =3469 (moisture) 2927 cm^{-1}, 2856 cm^{-1}, 1720 cm^{-1}, 1660 cm^{-1},1595 cm^{-1}, 1390 cm^{-1}, 1296 cm^{-1}. MS (MALDI) calculated is 759.29: Found: 759.295, Melting point: as can be seen from TGA profile (Supplementary Figure 17), ***S*-G** is stable until 350 °C, the melting point apparatus used can only measure up to 280 °C. Until this temperature, no melting of ***S*-G** was seen. Thus, we conclude that ***S*-G** has a melting point of >280 °C.

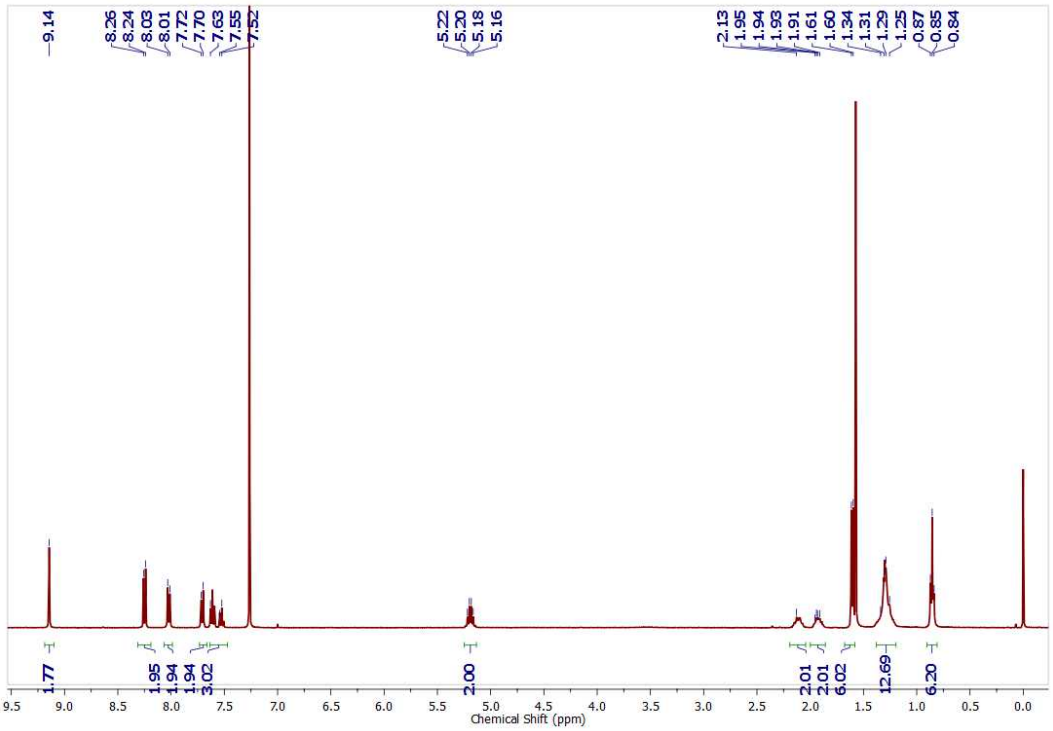

Supplementary Figure 5. ^{1}H-NMR characterisation. ^{1}H-NMR spectrum (400 MHz) of ***S*-G** in $CDCl_3$ (concentration: 2.5 mg in 0.5mL of $CDCl_3$).

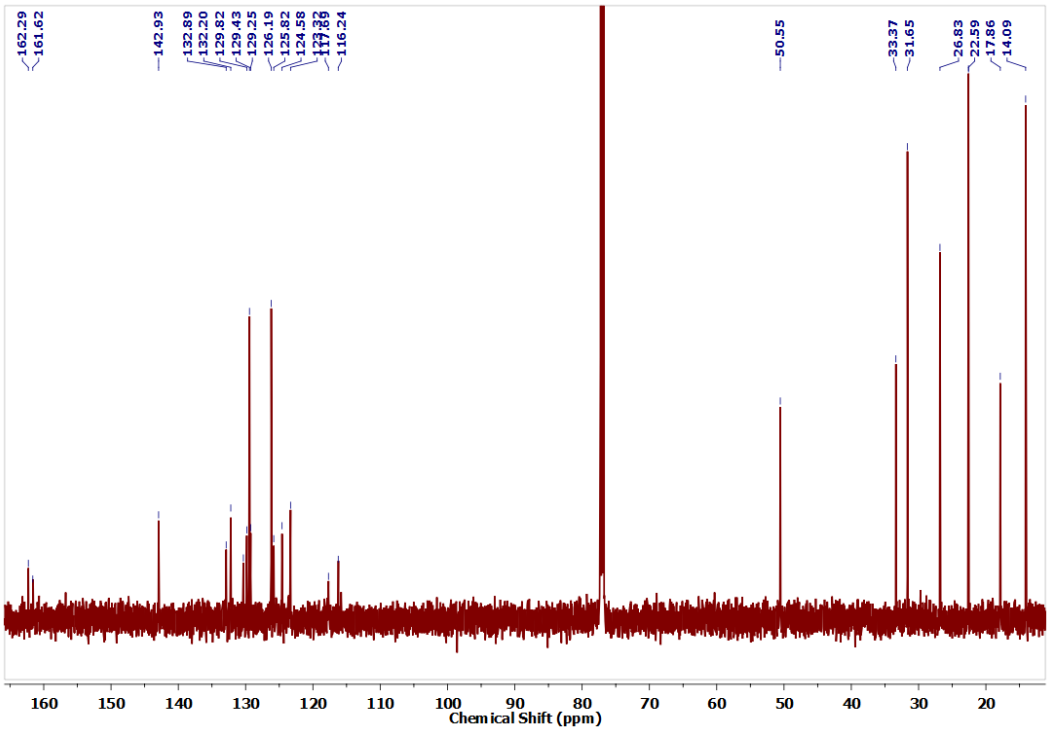

Supplementary Figure 6. ^{13}C-NMR characterisation. ^{13}C-NMR (150 MHz) spectrum of ***S*-G** in $CDCl_3$.

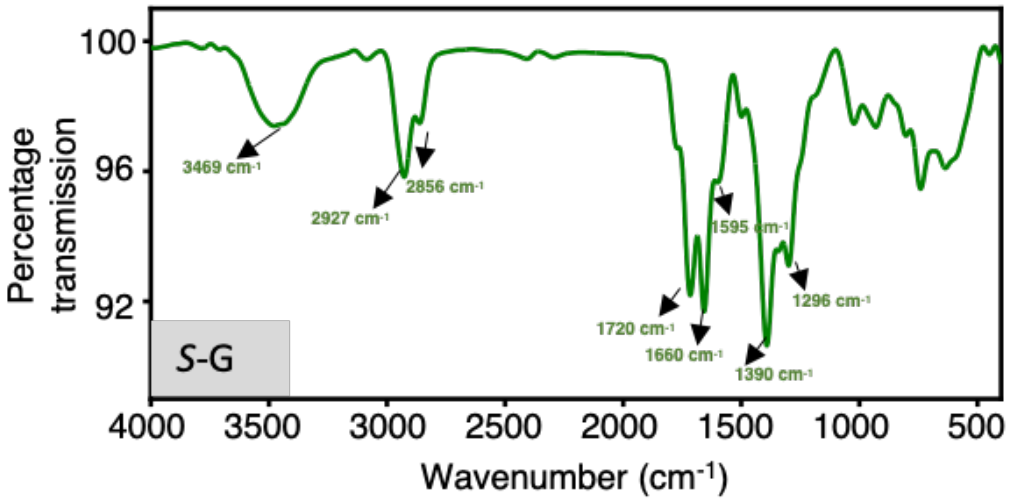

Supplementary Figure 7. FTIR spectrum of *S*-G. The peak near 3600 cm^{-1} is due to the presence of moisture in the KBr pellet. The peaks at 2927 cm^{-1} and 2856 cm^{-1} are due to the alkyl C-H stretching, 1720 cm^{-1} and 1660 cm^{-1} are due to carbonyl stretching (C=O), peak at 1595 cm^{-1} is due to aromatic C=C stretching, 1296 cm^{-1} is due to C-N stretching.

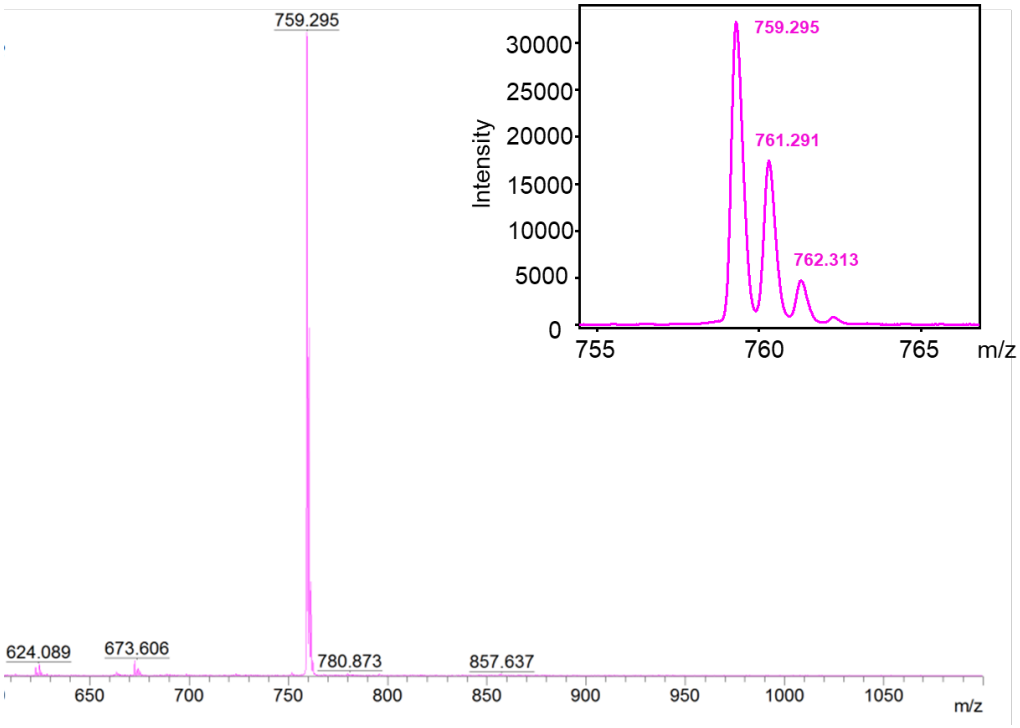

Supplementary Figure 8. MALDI-TOF analysis. MALDI-TOF Spectrum of ***S*-G**, (inset: zoomed in spectrum to show isotopic patterns).

Synthesis and characterisation of *R*-G

The synthesis of ***R*-G** was carried out in similar way to ***S*-G**. In brief, ***R*-PDI^2** (150 mg, 1 equivalent, 0.255 mmol), **4-Phenyl-1,2,4-triazolin-3,5-dione** (2) (223 mg, 5 equivalents, 1.278 mmol) and p-Chloranil (251 mg, 4 equivalents, 1.022 mmol) were taken in a 25 mL double-necked round bottom flask. It was then charged with anhydrous benzene (10 mL) and degassed by bubbling with nitrogen gas for over 30 min. It was refluxed at 80 ºC for a period of 7 days. The reaction mixture turned green. The reaction mixture was allowed to cool to room temperature to give precipitate, after which it was washed with hexane and acetone to yield a green coloured solid upon drying under reduced pressure[3]. Further purification of this was done by column chromatography on silica gel. The eluant used was 98:2 Chloroform: Acetone to afford the final green product, ***R*-G**. Yield: 62% (120 mg). It was characterised using various analytical techniques.^{1}H NMR was recorded at a concentration of 2.5 mg in 0.5 mL of $CDCl_3$. ^{1}H NMR (400 MHz, $CDCl_3$), δ 9.13 (s, 2H), 8.24 (d, J = 7.9 Hz, 2H), 8.00 (d, J = 8.0 Hz, 2H), 7.71 (d, J = 7.4 Hz, 2H), 7.61 (t, J = 7.7 Hz, 3H), 5.26 – 5.09 (m, 2H), 2.10 (d, J = 17.5 Hz, 2H), 1.93 (d, J = 13.1 Hz, 2H), 1.61 (d, J = 6.9 Hz, 6H), 1.31 (d, J = 17.6 Hz, 12H), 0.84 (s, 6H).^{13}C NMR (150 MHz, $CDCl_3$), δ (ppm): 162.14, 161.46, 142.90, 132.72, 132.10, 130.18, 129.77, 129.40, 126.21, 125.69, 124.45, 123.21, 117.49, 116.03, 50.57, 33.36, 31.65, 26.84, 22.60, 17.79, 14.10. IR (KBr) =3469 (moisture) 2926 cm^{-1}, 2856 cm^{-1}, 1720 cm^{-1}, 1660 cm^{-1}, 1595 cm^{-1}, 1390 cm^{-1}, 1297 cm^{-1}. MS (MALDI) calculated is 759.29: Found: 759.136. Melting point: as can be seen from TGA profile, ***R*-G** is stable until 350 °C (Supplementary Figure 17), the melting point apparatus used can only measure up to 280 °C. Until this temperature, no melting of ***R*-G** was seen. Thus we conclude that ***R*-G** has a melting point of >280 °C.

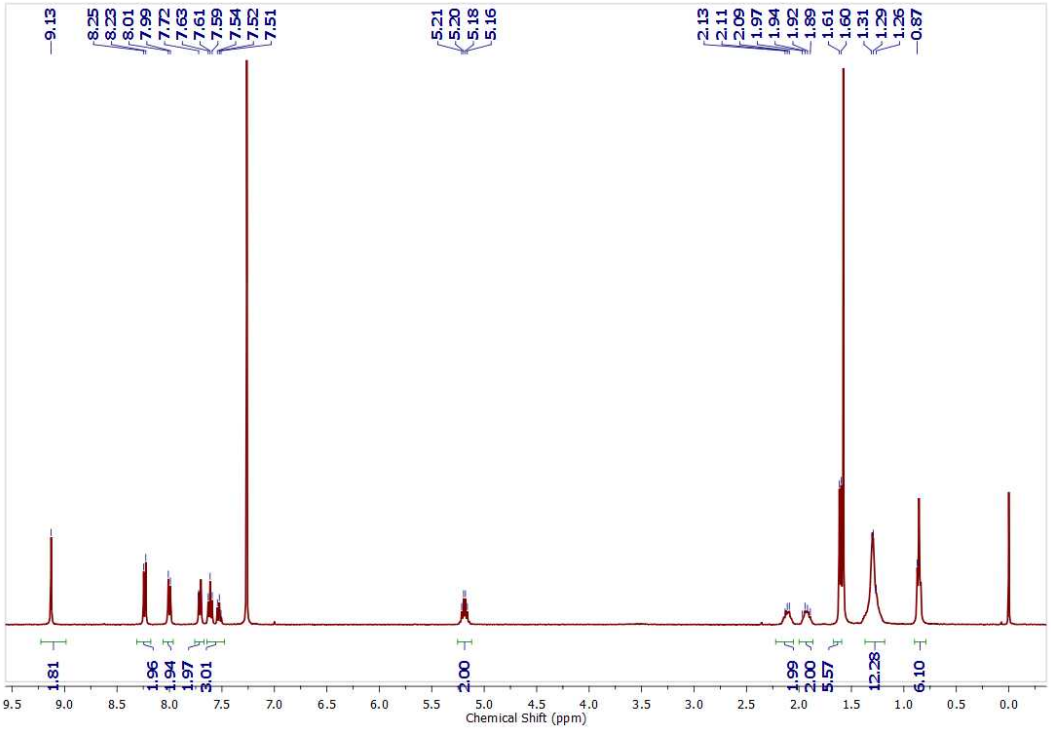

Supplementary Figure 9. ^{1}H-NMR characterisation. ^{1}H-NMR spectrum (400 MHz) of ***R*-G** in $CDCl_3$. (concentration: 2.5mg in 0.5 mL of $CDCl_3$).

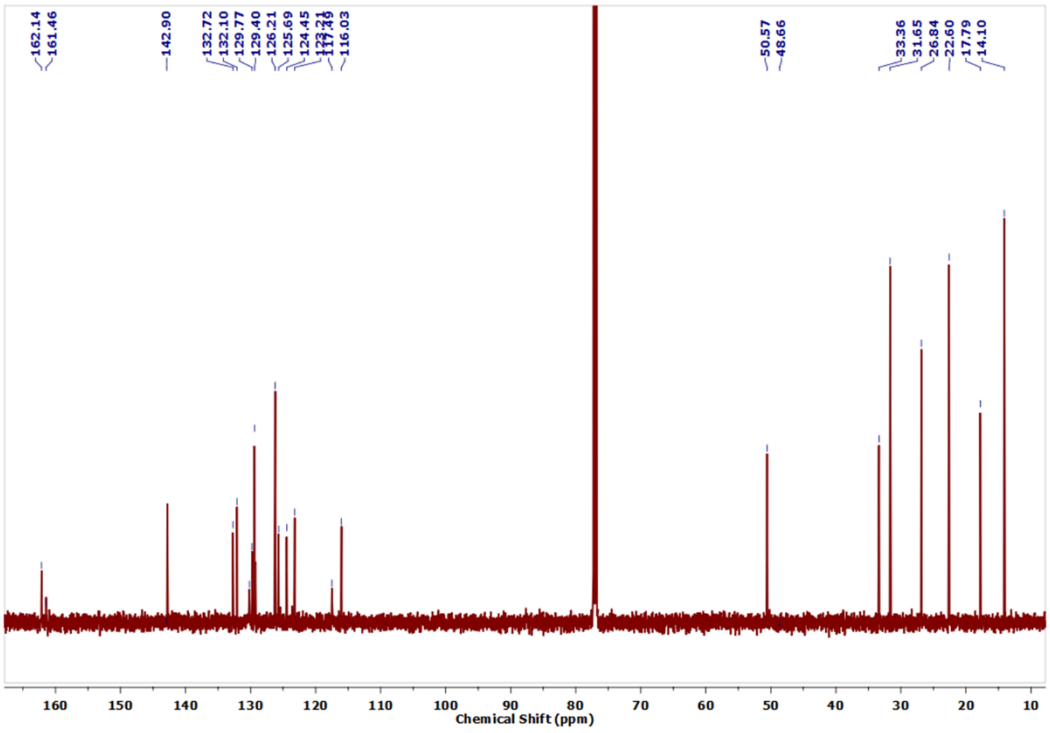

Supplementary Figure 10. ^{13}C-NMR characterisation. ^{13}C-NMR spectrum (150 MHz) of ***R*-G** in $CDCl_3$.

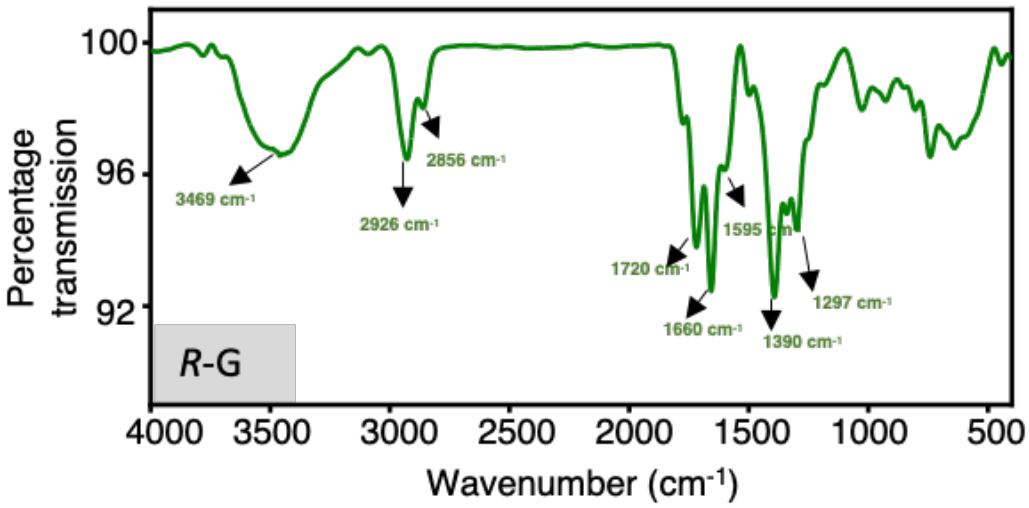

Supplementary Figure 11. FTIR spectrum of *R*-G. The peak near 3600 cm^{-1} is due to the presence of moisture in the KBr pellet. The peaks at 2926 cm^{-1} and 2856 cm^{-1} are due to the alkyl C-H stretching, 1720 cm^{-1} and 1660 cm^{-1} are due to carbonyl stretching (C=O), peak at 1595 cm^{-1} is due to aromatic C=C stretching, 1297 cm^{-1} is due to C-N stretching.

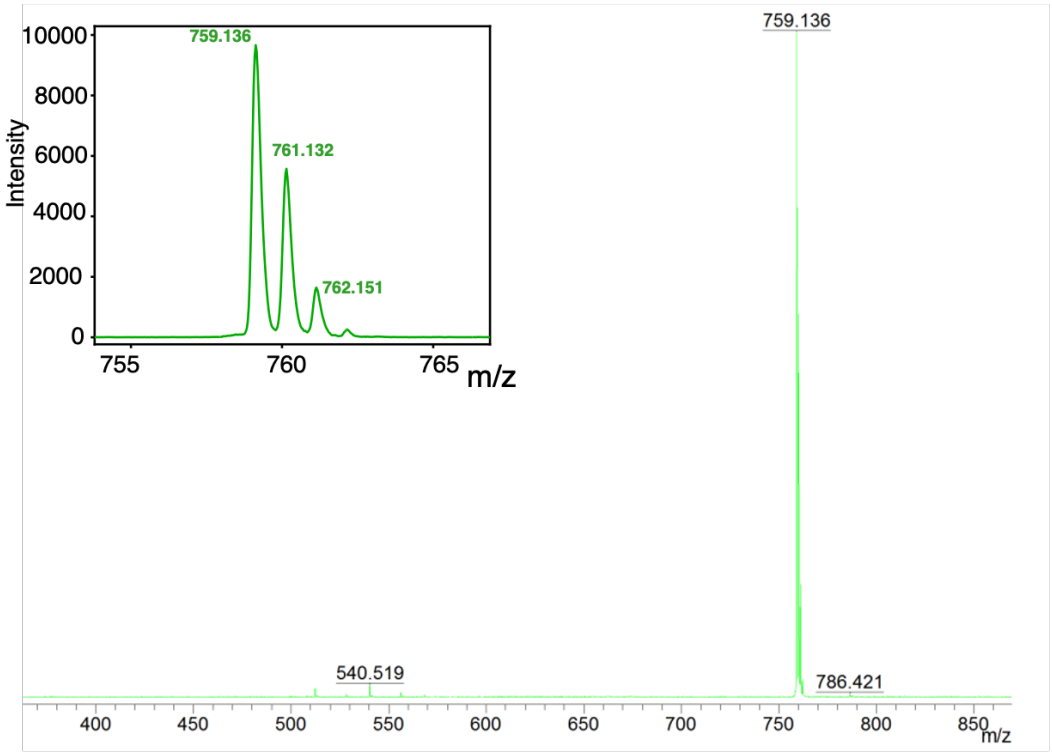

Supplementary Figure 12. MALDI-TOF analysis. MALDI-TOF Spectrum of ***R*-G** (inset: zoomed in spectrum to show isotopic patterns).

Synthesis and characterisation of *A*-G

The synthesis of ***A*-G** was carried out in similar way to ***S*-G**. In brief, **A-PDI**[1] (150 mg, 1 equivalent, 0.255 mmol), **4-Phenyl-1,2,4-triazolin-3,5-dione** (2) (223 mg, 5 equivalents, 1.278 mmol) and p-Chloranil (251 mg, 4 equivalents, 1.022 mmol) were taken in a 25 mL double-necked round bottom flask. It was then charged with anhydrous benzene (10 mL) and degassed by bubbling with nitrogen gas for over 30 min. It was refluxed at 80 ºC for a period of 7 days. The reaction mixture turned green. The reaction mixture was allowed to cool to room temperature to give precipitate, after which it was washed with hexane and acetone to yield a green coloured solid upon drying under reduced pressure[3]. Further purification of this was done by column chromatography on silica gel. The eluant used was 98:2 Chloroform: Acetone to afford the final green product, ***A*-G**. Yield: 68% (130 mg) It was characterised using various analytical techniques.^{1}H NMR was recorded at a concentration of 2.5 mg in 0.5 mL of $CDCl_3$. ^{1}H NMR (400 MHz, $CDCl_3$), δ 9.14 (s, 1H), 8.24 (d, *J* = 7.9 Hz, 1H), 8.01 (d, *J* = 8.1 Hz, 1H), 7.74 – 7.68 (m, 1H), 7.59 (dd, *J* = 25.3, 17.3 Hz, 2H), 5.19 (h, *J* = 6.9 Hz, 1H), 2.11 (dd, *J* = 20.7, 10.8 Hz, 1H), 1.98 – 1.86 (m, 1H), 1.61 (d, *J* = 6.9 Hz, 3H), 1.26 (d, *J* = 2.8 Hz, 7H), 0.85 (t, *J* = 7.0 Hz, 4H). ^{13}C NMR (150 MHz, CDCl3) δ 162.14, 161.43, 142.97, 132.72, 132.00, 129.77, 129.34, 129.25, 126.21, 125.69, 124.45, 123.24, 117.53, 116.03, 50.57, 33.30, 31.65, 26.84, 22.60, 17.74, 14.10. IR (KBr) =3424 (moisture) 2927 cm^{-1}, 2857 cm^{-1}, 1720 cm^{-1}, 1660 cm^{-1}, 1595 cm^{-1} 1389 cm^{-1}, 1295 cm^{-1}. MS (MALDI) calculated is 759.29: Found: 759.012. Melting point: as can be seen from the TGA profile (Supplementary Figure 17), A-G is stable until 350 °C, the melting point apparatus used can only measure up to 280 °C. Until this temperature, no melting of ***A*-G** was seen. Thus we conclude that ***A*-G** has a melting point of >280 °C.

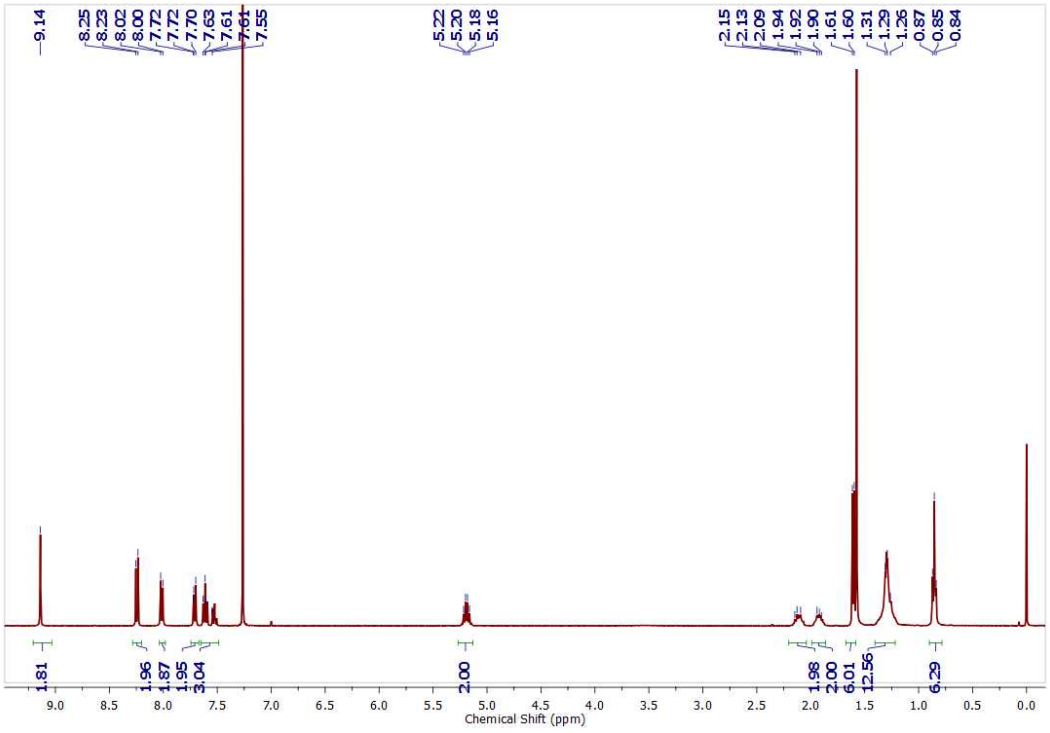

Supplementary Figure 13. ^{1}H-NMR characterisation. ^{1}H-NMR (400 MHz) spectrum of ***A*-G** in $CDCl_3$. (concentration: 2.5mg in 0.5 mL of $CDCl_3$).

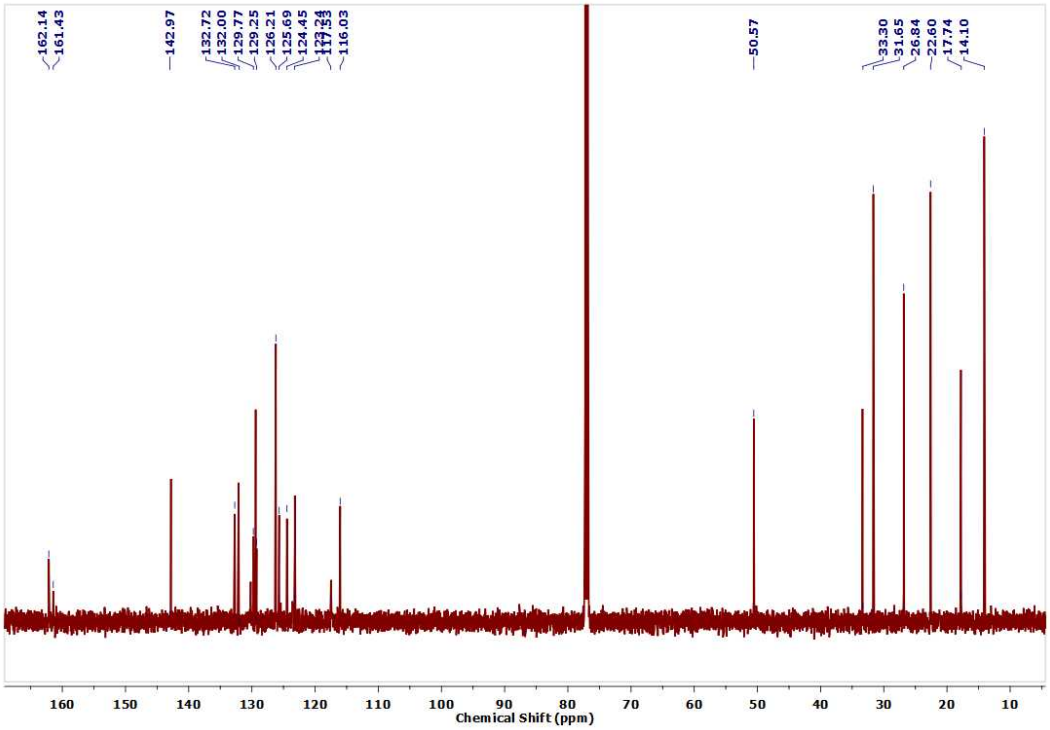

Supplementary Figure 14. ^{13}C-NMR characterisation. ^{13}C-NMR (150 MHz) spectrum of ***A*-G** in $CDCl_3$.

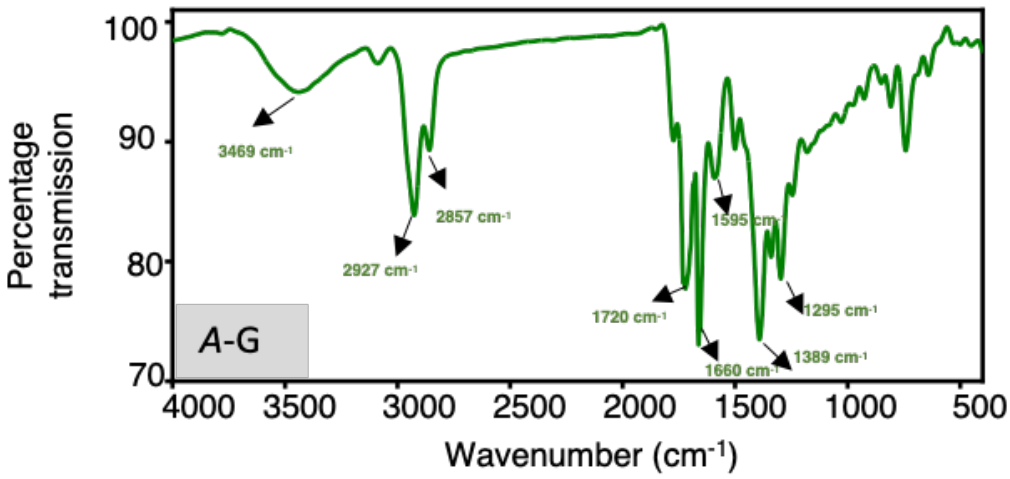

Supplementary Figure 15. FTIR spectrum of *A*-G. The peak near 3600 cm^{-1} is due to the presence of moisture in the KBr pellet. The peaks at 2927 cm^{-1} and 2857 cm^{-1} are due to the alkyl C-H stretching, 1720 cm^{-1} and 1660 cm^{-1} are due to carbonyl stretching (C=O), peak at 1595 cm^{-1} is due to aromatic C=C stretching, 1295 cm^{-1} is due to C-N stretching.

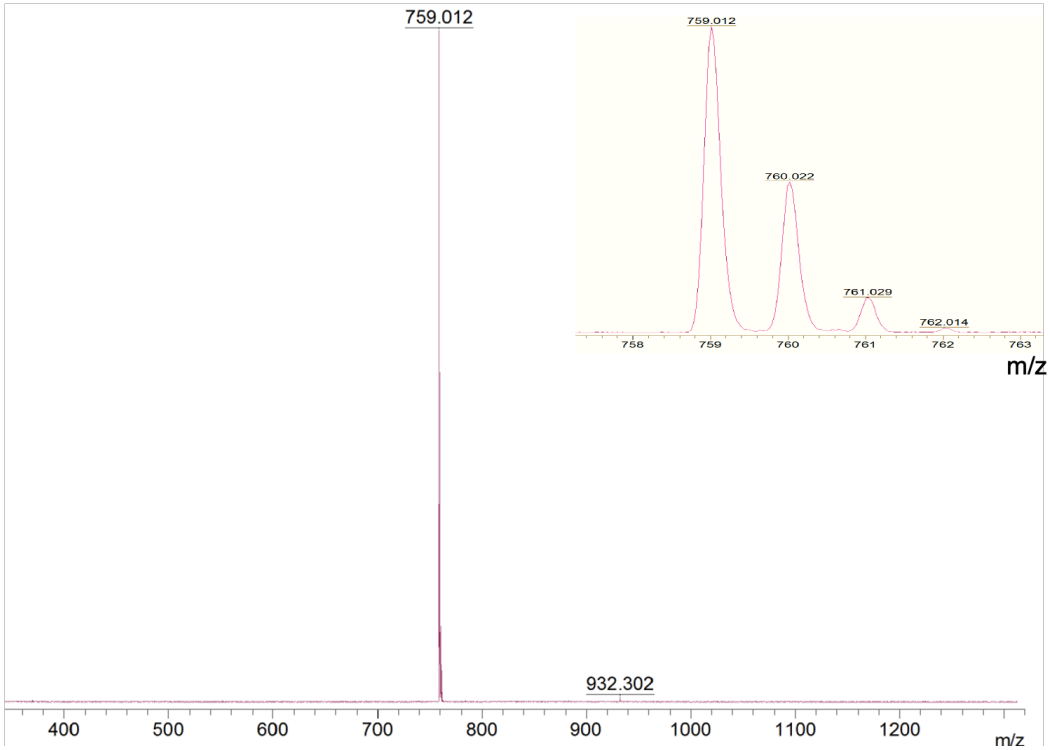

Supplementary Figure 16. MALDI-TOF analysis. MALDI-TOF Spectrum of ***A*-G** (inset: zoomed in spectrum to show isotopic patterns).

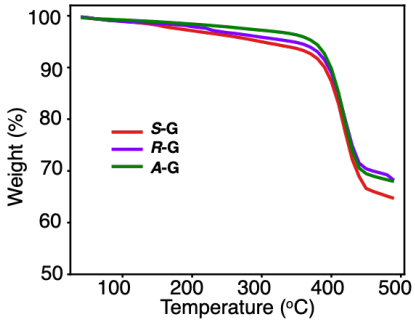

Supplementary Figure 17. Thermogravimetric analysis. TGA profile of ***S*-G** (red curve), ***R*-G** (purple curve) and ***A*-G** (green curve) measured under N_2 gas flow of 100 mL min^{-1} and heating rate of 10 °C min^{-1}.

Supplementary Note 3: Mathematical modelling-

The mathematical fitting of kinetics of aggregation was done using the amylofit software, which is developed by Knowles and group[4]. The initial aggregation kinetics of different concentrations are loaded into the program from which half lifetimes and the scaling exponent value (γ) from double logarithmic plot of concentration and half lifetimes is obtained. The half-time is the value where half of the monomer concentration is aggregated and the remaining half is as such. Thus this can be traced as a point that is middle of initial beginning of aggregation and saturation of curve after aggregation. The half-time of aggregation is dependent on the initial concentration of monomers by the relation-

$$t_{1/2} = m_0^{\gamma}$$

where γ is the scaling exponent. A double logarithmic plot of the equation is used to estimate γ value from its slope ;

$$\log(t_{1/2}) = \gamma \log(m_0) + C$$

The γ value is used to obtain the relation order constants n_1 and n_2, primary and secondary nucleation reaction order constants respectively, which are related by the following equations-

$$n_1 = -\gamma/2$$

$$n_2 = -(2\gamma+1)$$

In the case of aggregation kinetics of ***S*-G,** γ obtained is -2.264, by fitting into 4 data points. Obtaining γ value nearly 2.5, we consider $n_2 = 4$ and $n_c = 3$.

Using these values, the aggregation kinetic profiles were fit into different self-assembly mechanisms and best fit with minimal mean square error (MSE) was obtained for 'Secondary nucleation dominated, unseeded'. The mathematical model for the program is-

The differential equations describing the system are-

$$\frac{dP}{dt} = k_n m(t)^{n_c} + k_2 m(t)^{n_2} M(t)$$

$$\frac{dM}{dt} = 2m(t)k_+ P(t)$$

The approximate analytical solution is-

$$\frac{M}{M_\infty} = 1 - \left(1 - \frac{M_0}{M_\infty}\right) e^{-k_\infty t} \cdot \left(\frac{B_- + C_+ e^{\kappa t}}{B_+ + C_+ e^{\kappa t}} \cdot \frac{B_+ + C_+}{B_- + C_+}\right)^{\frac{k_\infty}{\kappa k_\infty}}$$

Where the definitions of parameters are-

$$\kappa = \sqrt{2 m_0 k_+ m_0^{n_2} k_2}$$

$$\lambda = \sqrt{2 k_+ k_n m_0^{n_c}}$$

$$C_{\pm} = \frac{k_+ P_0}{\kappa} \pm \frac{k_+ M_0}{2 m_0 k_+} \pm \frac{\lambda^2}{2\kappa^2}$$

$$k_\infty = \sqrt{(2k_+ P(0))^2 + \frac{4k_+ k_n m_0^{n_c}}{n_c} + \frac{4k_+ k_2 m_{tot} m_0^{n_c}}{n_2} + \frac{4k_+ k_2 m_0^{n_2+1}}{n_2 + 1}}$$

$$k^-_\infty = \sqrt{k_\infty^2 - 2C_+ C_- \kappa^2}$$

$$B_{\pm} = \frac{k_\infty \pm k^-_\infty}{2\kappa}$$

where the mass at long times, M∞, is the total protein mass concentration, m_{tot}. This solution is more accurate than the ones involving fragmentation, i.e. very close to the numerical integration of the differential equations, however it only applies for negligible off rates k_{off} $k_+ m_0$.

Parameters involved in the above equations are –

P = Fiber number concentration (number concentration of supramolecular polymer)

M_0 = Fiber mass concentration (mass concentration of supramolecular polymer)

m_0 = Monomer concentration

k_n = Primary nucleation rate constant

k_2 = Secondary nucleation rate constant

k_+ = Elongation rate constant

n_1 = reaction order of primary nucleation

n_2 = reaction order of secondary nucleation.

The fitting parameters used to obtain best fit as shown in 4b and 4c are $k_+ k_n = 1 \times 10^6$, $k_+ k_2 = 1 \times 10^{18}$.

Supplementary Note 4: Computational details

To investigate the structural differences and fundamental interactions governing the stability of the ***S*-G** and ***S*-PDI** stacks, we performed molecular dynamics (MD) simulations. Since experiments showed that both ***R*** and ***S*** stereogenic monomers exhibit similar properties, we selected the ***R*** stereogenic monomer for building the stacks. However, as most of the experimental results focused on the ***S*-G** stack, we use the label ***S*-G** for clarity and consistency. Initially, the lowest energy dimers were identified by using four order parameters (Supplementary Figure 18a) to generate multiple dimer configurations, which were then subjected to geometry optimization using the semi-empirical GFN2-xTB method[5]. The corresponding dimer configurations and their energies for each stack are shown in Supplementary Figure 18b. Next, the lowest energy dimer of each molecule was further optimized using density functional theory at the ωB97XD/6-31G(d) level of theory. These optimized configurations were subsequently used for second-generation absolutely localized molecular orbital-based energy decomposition analysis (ALMO-EDA) to break down the intermolecular interaction energy into physically meaningful and chemically intuitive components, as implemented in Q-Chem 5.2 [6-8]. Under the ALMO-EDA scheme, the total intermolecular interaction energy is decomposed into five meaningful energy components such as attractive electrostatic, dispersion, polarization, charge transfer and repulsive Pauli interactions.

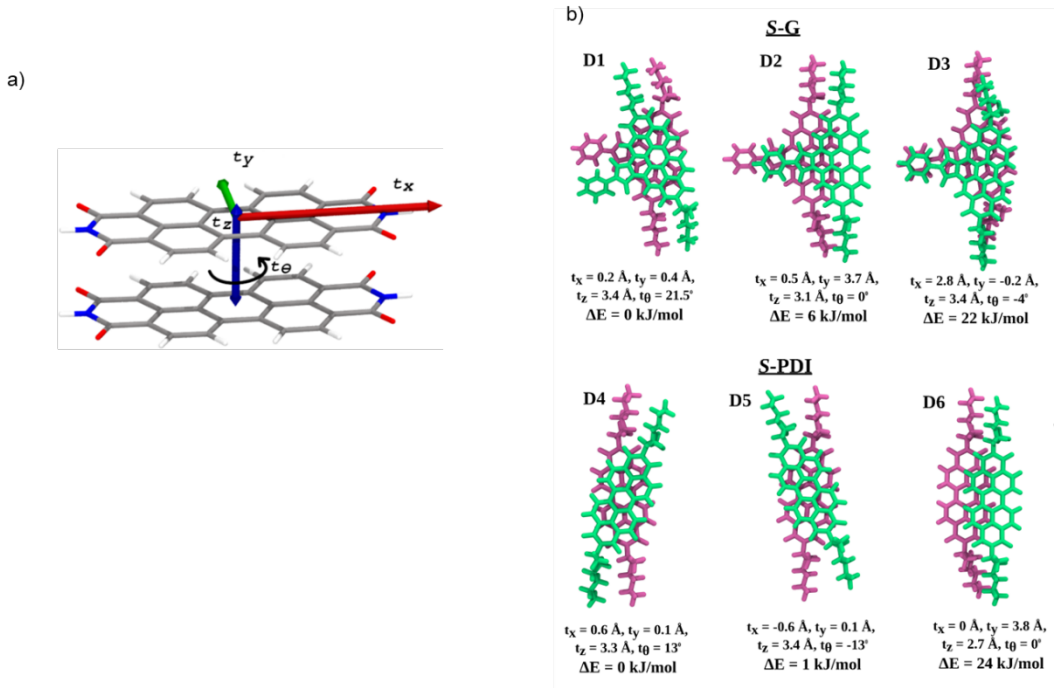

Supplementary Figure 18. Lowest-energy dimer configurations. (a) Schematic illustration of the four order parameters (t_x , t_y , t_z and t_θ) associated with monomer stacking. These parameters represent displacements along the long molecular axis (t_x), short molecular axis (t_y), π-π stacking distance (t_z) and intermolecular twist angle (t_θ). (b) Optimized lowest-energy dimer configurations for (D1–D3) ***S*-G** and (D4–D6) ***S*-PDI**. In D1 and D3, the second monomer is rotated to avoid tail-tail steric clashes, with D3 exhibiting a lower degree of rotation, leading to relatively higher repulsive energy. D2 adopts a stair-step geometry, where the second monomer is translated along both the short and long molecular axes. D4 and D5 represent twisted dimers, while D6 exhibits a stair-step configuration.

Helical stacks of P-helicity corresponding to ***S*-G** and ***S*-PDI**, each containing 24 monomers, were then constructed for solvent-phase molecular dynamics simulations. The binding energies of these stacks in the gas phase were calculated using a force field to compare their stability. Our results indicate

that ***S*-G** stack is more stable than the ***S*-PDI** stack. All classical molecular dynamics simulations were performed using the GROMACS package (version 2022) [9,10]. The GAFF potential[11,12] was applied to model the solutes ***S*-G** and ***S*-PDI**, as well as the solvent molecules chloroform and IPA, while atomic partial charges were derived using the AM1-BCC method via AmberTools24 [11-13]. The ACPYPE tool was used to convert the AMBER simulation files into GROMACS-compatible formats[14]. We prepared two systems in which preformed stacks of ***S*-G** and ***S*-PDI** were immersed in a chloroform and IPA mixture (15:85 v/v). Each simulation box contained 1,792 chloroform molecules and 10,645 IPA molecules surrounding the polymer stack. A series of steps were followed to generate optimal initial configurations for each system, which were then used for molecular dynamics simulations. First, the stacks were energy minimized using the steepest-descent algorithm before introducing the solvent into the simulation box. The systems were then energy minimized again and underwent an equilibration process, detailed as follows: With the stack frozen, simulated annealing (300K–450K–300K) was performed for 300 ps in the NVT ensemble. Following this, a 5 ns NVT simulation was run at 298 K using velocity rescaling[15] for temperature coupling while keeping the stack frozen. The systems were then equilibrated in the NPT ensemble at 298 K, using Berendsen[16] pressure coupling with a 5 ps time constant over 10 ns, applying position restraints on the stack's heavy atoms. Next, the restraints on the stack were removed, and the systems were subjected to a 1 ns cooling process, reaching a temperature of 50 K. Following this, a 5 ns NVT simulation was performed to bring the temperature back to 298 K. Subsequently, 20 ns of simulations were run using the Berendsen pressure bath with a time constant of 5 ps and temperature coupling via the velocity rescaling thermostat, with a time constant of 1 ps. Finally, a 300 ns trajectory was generated in the NPT ensemble for analysis. The equations of motion were integrated using the leap-frog algorithm[17] with a time step of 2 fs. Lennard-Jones and Coulomb interactions were scaled by factors of 0.5 and 0.8333, respectively, with a spherical cut-off of 12 Å applied to short-range non-bonded interactions. Long-range electrostatic interactions were computed using the Particle Mesh Ewald (PME) method[18] All bonds involving hydrogen atoms were constrained to their equilibrium values using the LINCS algorithm[19]. Atomic coordinates were saved at 1 ps intervals. VMD was used for trajectory visualization and plotting[20], and matplotlib was employed for graph plotting[21,22].

2. Supplementary Figures

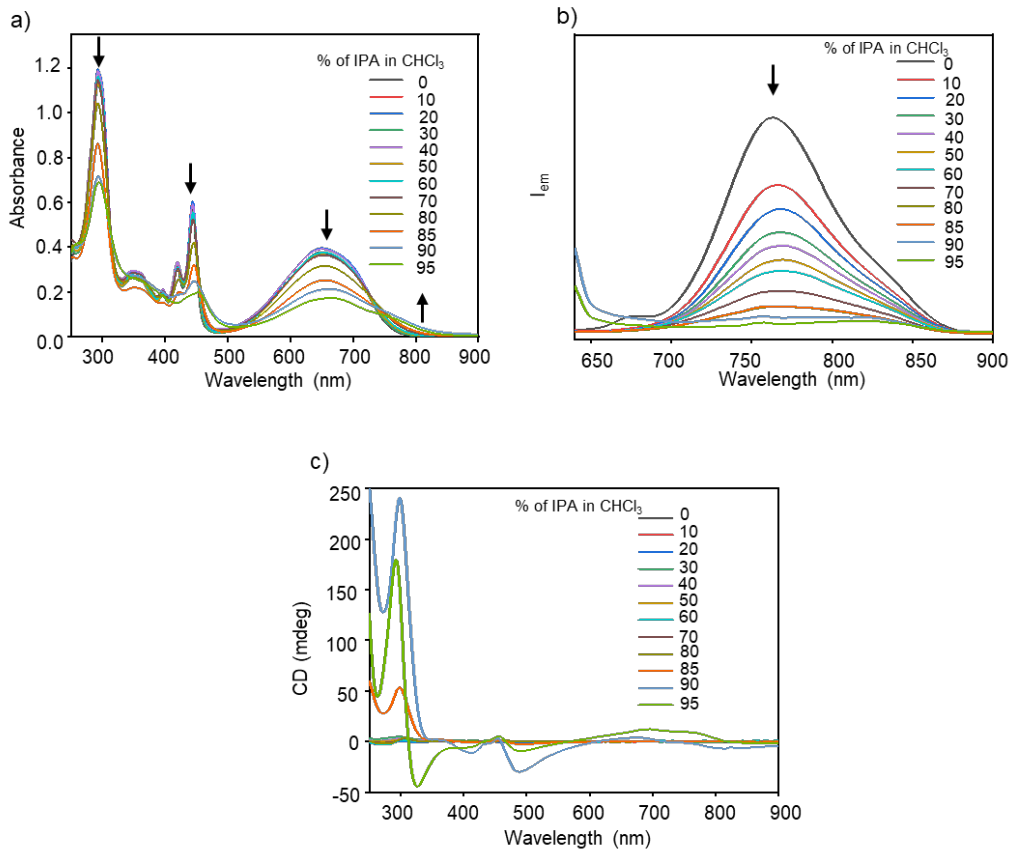

Supplementary Figure 19. **Optical properties of *S*-G.** (a) Electronic absorption and (b) fluorescence spectra of a 30 μM solution of ***S*-G** at various vol% $CHCl_3$ in IPA (l = 1 cm, λ_{ex}= 620 nm). The fluorescence intensity was corrected for the differences in the absorbance. (c) Circular Dichroism spectra of a 30 μM solution of ***S*-G** at various vol% $CHCl_3$ in IPA (l = 1 cm).

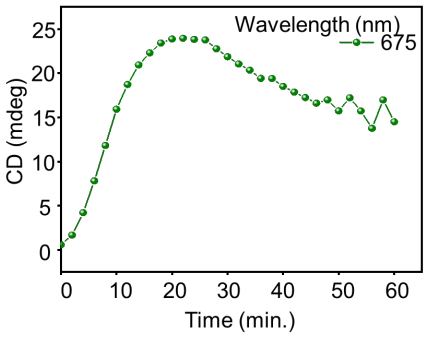

Supplementary Figure 20. Variation of Circular dichroism (CD) signal at 675 nm with time. Time-dependant CD spectrum of a 30 μM solution of ***S*-G** in 15 vol% $CHCl_3$ in IPA (l = 1 cm) monitored at 675 nm. An increase in CD intensity was observed in the beginning due to hierarchical assembly and later decreased due to the precipitation of large-sized higher order assemblies from the solution.

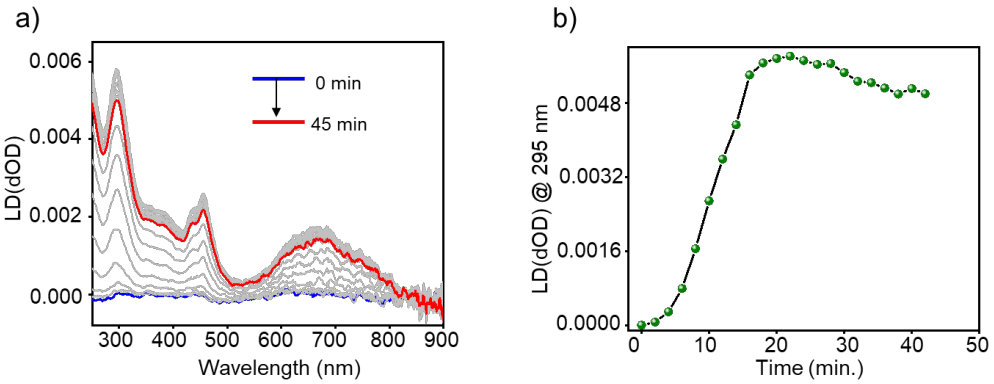

Supplementary Figure 21. Time dependant linear dichroism spectrum. (a) Time dependant linear dichroism spectra of a 30 μM solution of ***R*-G** in 15 vol% $CHCl_3$ in IPA monitored over a time period of 45 min. (b) A plot of variation of LD signal at 295 nm versus time.

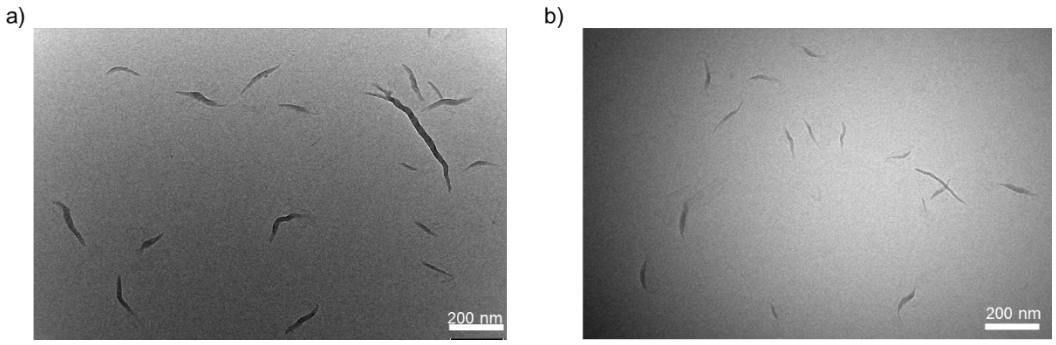

Supplementary Figure 22. TEM characterisation of *S*-G. TEM images of a) and b) freshly prepared solutions of 30 μM ***S*-G** in 15% $CHCl_3$ in IPA. These two images were taken at two different areas of the TEM grid.

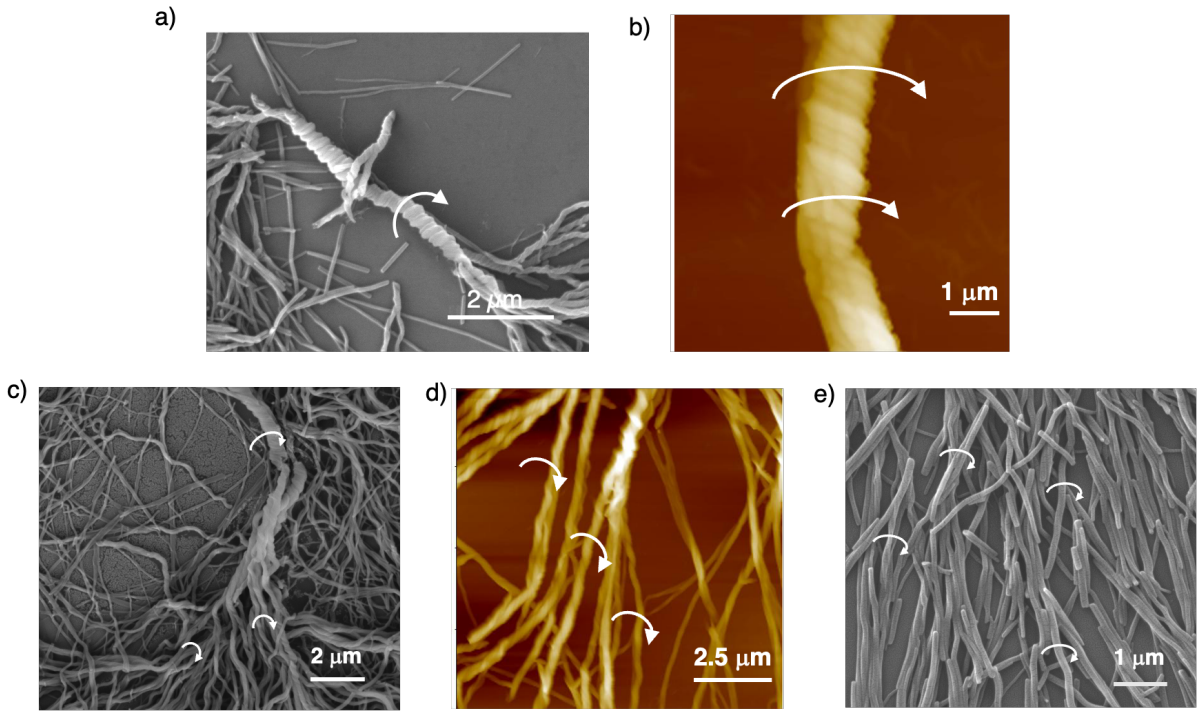

Supplementary Figure 23. Microscopy characterisation of DHS of *S*-G. FE-SEM and AFM images of DHS of ***S*-G** showing righthanded homochirality. (a) FE-SEM and (b) AFM images of superhelix of DHS of ***S*-G**. **(**c) FE-SEM image of branches in DHS showing righthanded helicity. (d) AFM and (e) FE-SEM images of thin helical fibers of DHS. These samples are prepared by spin-coating a 30 μM solution of ***S*-G** in 15% $CHCl_3$ in IPA on a silicon wafer.

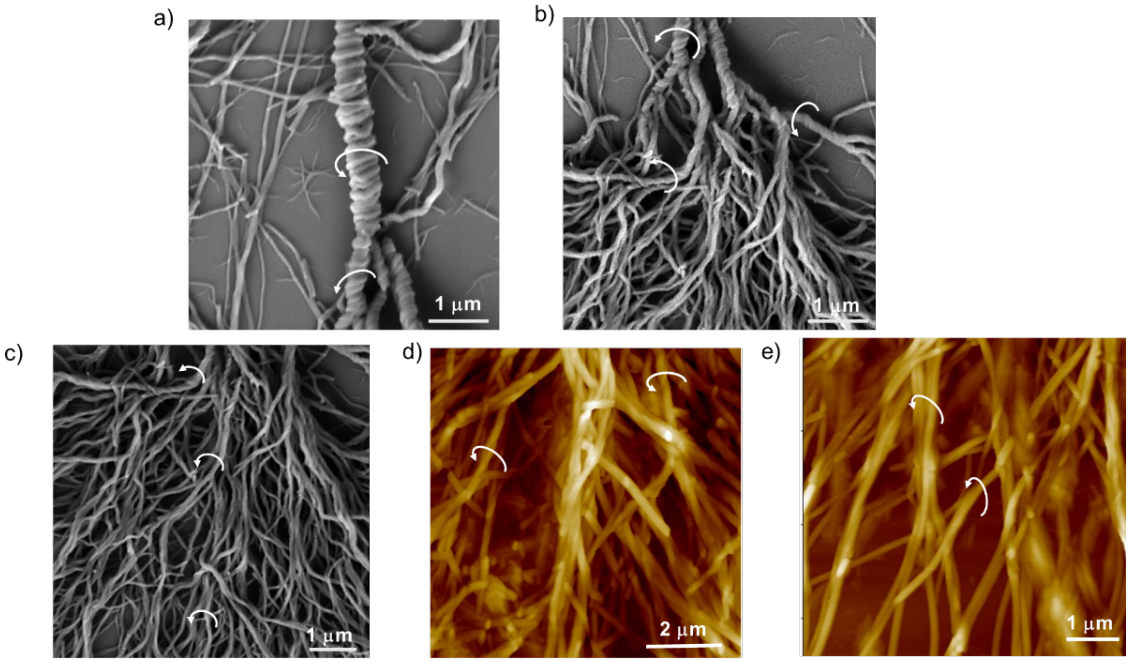

Supplementary Figure 24. Microscopy characterisation of DHS of *R*-G. FE-SEM images and AFM images of DHS of ***R*-G** showing lefthanded chirality and homochirality. (a) FE-SEM image of superhelix of DHS of ***R*-G**. (b) FE-SEM image of branches of DHS of ***R*-G**. (c) FE-SEM image of branches and thin fibers showing homochirality in DHS of ***R*-G**. (d) and (e) AFM images of thin helical fibers of DHS. These samples are prepared by spin-coating a 30 μM solution of ***R*-G** in 15% $CHCl_3$ in IPA on a silicon wafer.

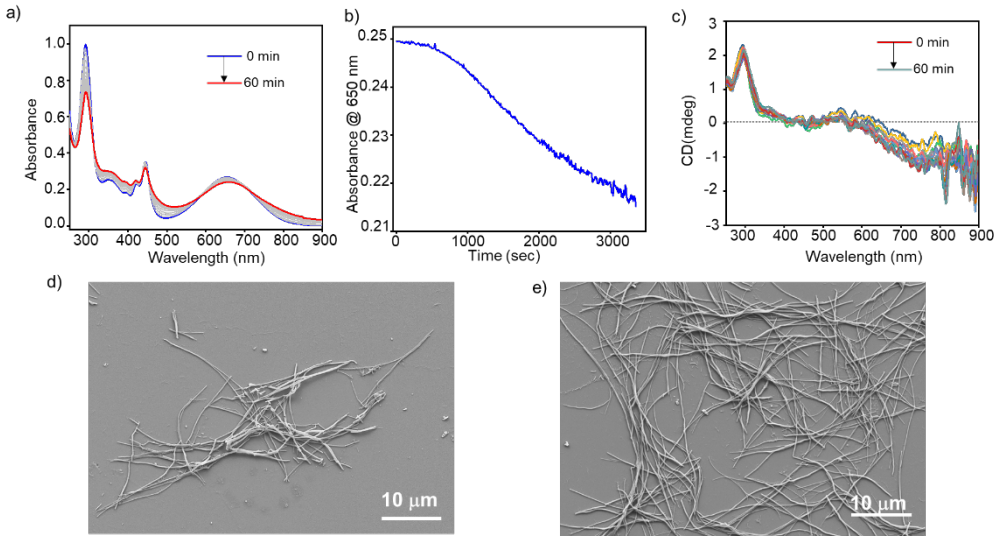

Supplementary Figure 25. Probing time dependant self-assembly of *A*-G. (a) Variation in absorption spectra of 30 μM solution of ***A*-G** in 15% $CHCl_3$ in IPA. (b) kinetics of aggregation of ***A*-G** monitored at 650 nm. (c) Time dependant CD spectra show no variation with increasing aggregation. (d) and (e) FE-SEM images of aggregates of ***A*-G** obtained after 3600 sec.

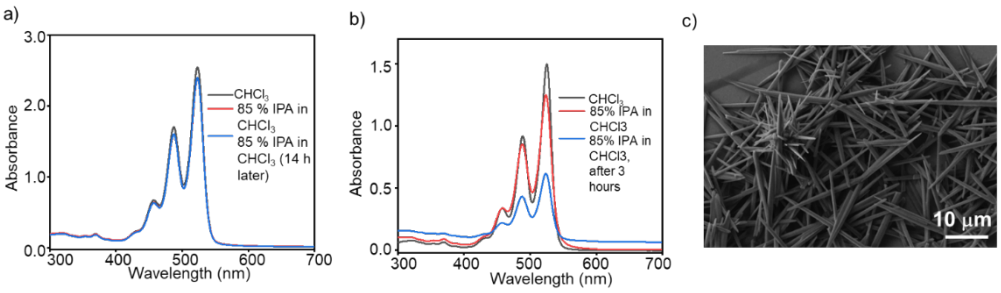

Supplementary Figure 26. Probing time-dependent self-assembly of *S*-PDI. (a) Absorption spectra of a 30 µM solution of ***S*-PDI** (l = 1 cm). (b) Absorption spectra of a 200 µM solution of ***S*-PDI** (l = 1 mm). (c) FE-SEM image of 200 µM solution of ***S*-PDI** in 15 % $CHCl_3$ in IPA in spin-coated on a silicon wafer.

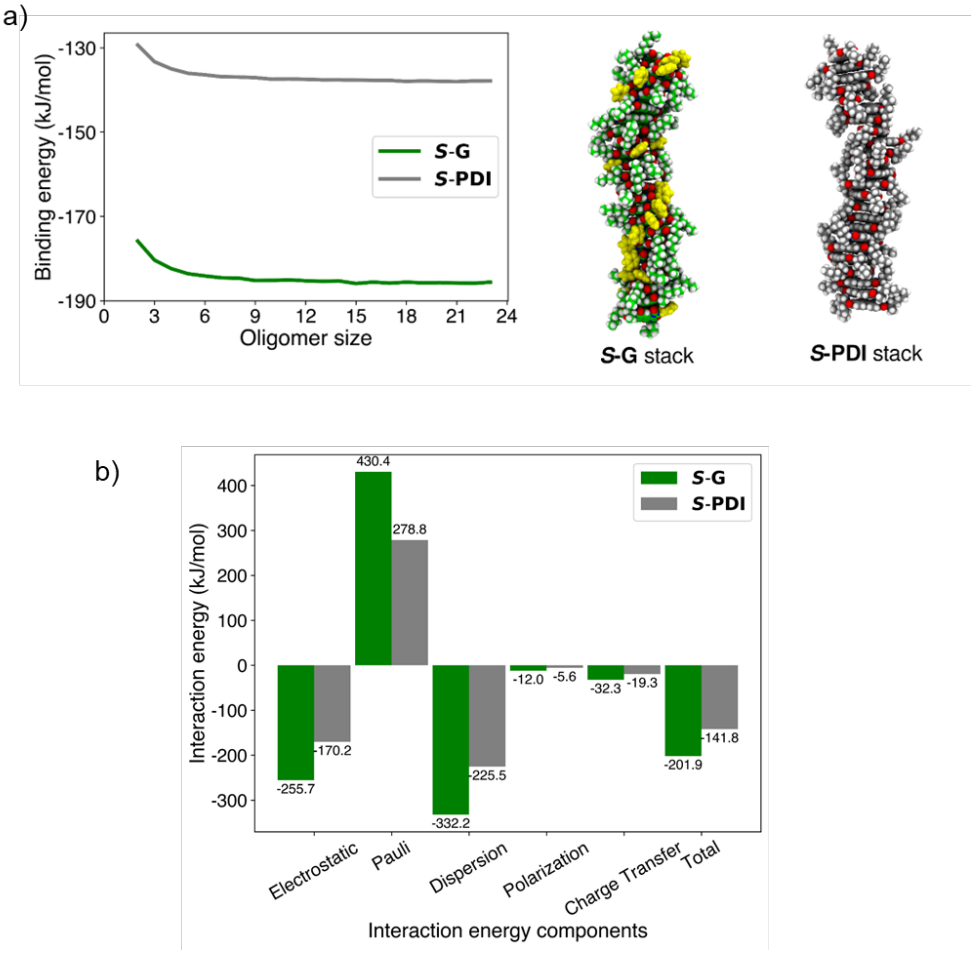

Supplementary Figure 27. MD simulations. (a) Gasphase force field binding energies of ***S*-G** and ***S*-PDI** stacks. The binding energies are calculated using the equation: $(E_n - E_1)/(n-1)$. Results show that the ***S*-G** stack is approximately 50 kJ/mol more stable than the ***S*-PDI** stack. Snapshots of the ***S*-G** and ***S*-PDI** stacks obtained from the equilibrium trajectories are shown on the right side. (b) Energy decomposition analysis of the lowest energy dimers in the gas phase for both ***S*-G** and ***S*-PDI**. This analysis was conducted using the ALMO-EDA framework at the ωB97XD/6-31G(d) level of theory.

Our results indicate that ***S*-G** stack is more stable than the ***S*-PDI** stack (Supplementary Figure 27a). In the most stable dimers (D1, D2, D4, & D5), one monomer is either rotated by approximately 20° relative to the geometric centre of the aromatic ring plane of the other monomer or translated along its short molecular axis, thereby minimizing steric repulsions from the branched methyl groups. Additionally, the alkyl chains of the two monomers are positioned slightly apart, interacting mainly through London dispersion forces[23], with most intermolecular C - - C distances exceeding 5 Å. This leads to a reduced contribution from the alkyl chains to dimer stabilization, as the branched methyl groups discourage strong interactions between the alkyl chains of neighbouring molecules in the stack. In the case of the ***S*-G** dimer, the two phenyl rings interact with each other, providing additional stabilization to the dimer. Energy decompositions based on the ALMO-EDA method for the ***S*-G** and ***S*-PDI** dimers, as illustrated in Supplementary Figure 27b, indicate that the stronger interactions among ***S*-G** monomers primarily arise from the presence of a bay-substitution group in the ***S*-G** molecule. It enhances the stability of the ***S*-G** dimer by considerably strengthening the electrostatic, dispersion, and charge transfer interactions. In contrast, the absence of this functional group in ***S*-PDI**s results in their self-assembly at relatively higher concentrations, primarily due to their weaker intermolecular interactions compared to those of ***S*-G** molecules.

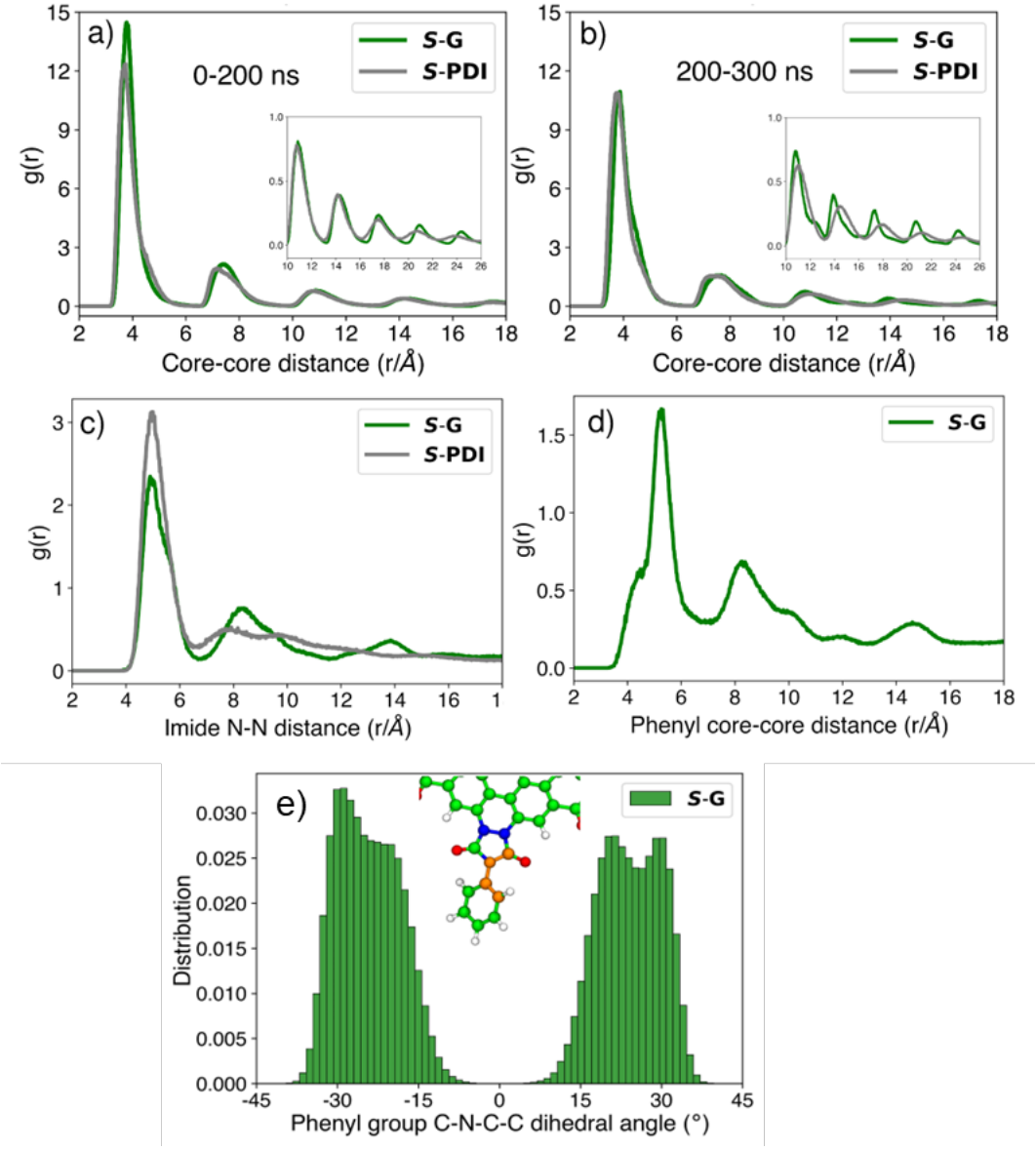

Supplementary Figure 28. Radial distribution functions. The radial distribution function (g(r)) between the geometric centers of the central ring of the aromatic core: (a) derived from the 200 ns MD trajectories, and (b) from an additional 100 ns MD trajectory for both ***S*-G** and ***S*-PDI** stacks. Additionally, (c) shows g(r) between the imide nitrogen atoms and (d) between the geometric centers of the phenyl rings. (e) Distribution of the dihedral angle C-N-C-C (highlighted in orange) associated with the phenyl ring.

To investigate the influence of solvent and temperature on the stacking propensity and orderliness in the extended fiber, all-atom classical molecular dynamics simulations are conducted on preform stacks in an explicit solvent mixture of chloroform and isopropyl alcohol (IPA) at a ratio of 15:85 (v/v), consistent with experimental conditions. Supplementary Figure 28a displays the radial distribution function (g(r)) between the geometric centers of the central ring of the aromatic core, derived from the 200 ns molecular dynamics trajectories (following equilibration). The presence of strong peaks in both systems indicates that both ***S*-G** and ***S*-PDI** stacks are stable in solution[24]. Importantly, the intensity of the first peak is higher for ***S*-G**, suggesting a greater stacking propensity

compared to S-PDI stacks. The g(r) calculated for the additional 100 ns of the trajectory (from 200 to 300 ns) reveals the emergence of long-range order in the structures of ***S*-G** compared to ***S*-PDI** (Supplementary Figure 28b). The short-range order evident in the initial 200 ns of the trajectory transitions into long-range order in the subsequent stages, thereby enhancing the stability and organization of the ***S*-G** stacks. This observation is further supported by the g(r) of the imide nitrogen-nitrogen distance (Supplementary Figure 28c), which exhibits well-defined second and third peaks for the ***S*-G** stack. To explore the origin of the higher orderliness and stability in the ***S*-G** stacks, we analyzed the role of the bay-substituted phenyl ring by assessing its flexibility relative to the larger aromatic core (Supplementary Figure 28e), as well as the g(r) of phenyl core-core distances (Supplementary Figures 28d and Figure 4a). The phenyl rings exhibit dynamic behaviour, tending to adopt a slanted orientation with an average angle of approximately ±25° relative to the aromatic core (Supplementary Figure 28e).

The g(r) of phenyl core-core distances displays two peaks at 5.2 Å and 8.2 Å, with a shoulder at 4.3 Å. From the visualization of the MD trajectories, the phenyl rings are observed to engage in three distinct types of interactions within the S-G stack: first, π-π interactions between neighbouring phenyl rings, corresponding to the shoulder at 4.3 Å in the g(r); second, CH-π interactions between adjacent phenyl rings, leading to the peak at 5.2 Å; and third, CH-π interactions between the branched methyl group of one molecule and the phenyl ring of a neighbouring molecule, resulting in the peak at 8.2 Å (Main text Figure 4a). As a result, the bay-substitution in the ***S*-G** stack leads to improved ordering and stabilization compared to the ***S*-PDI** stack.

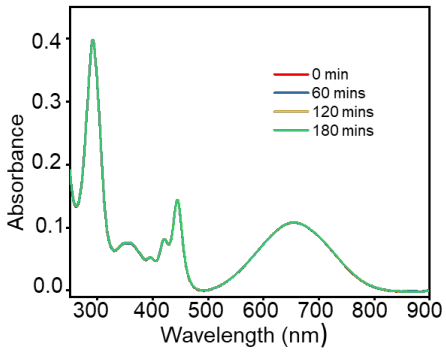

Supplementary Figure 29. Time-dependent absorption spectra of 10 µM solution of *S*-G. Absorption spectra of a 10 µM solution of ***S*-G** in 15% $CHCl_3$ in IPA, monitored over a period of 180 min. (3 hours).

The aggregation kinetics fit into primary nucleation yielded poor fit with greater MSE as shown below-

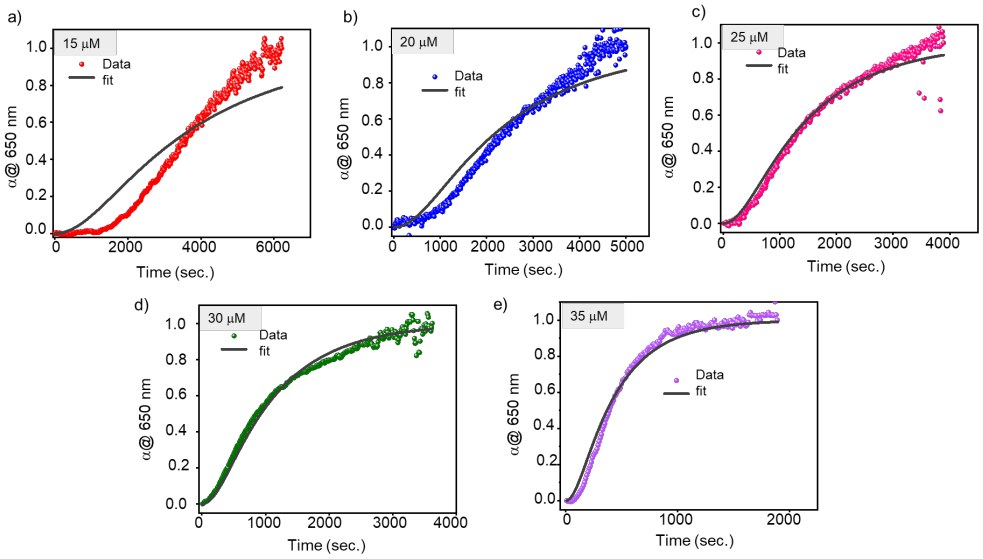

Supplementary Figure 30. Kinetic analysis of aggregation of *S*-G using primary nucleation elongation model. Kinetic profiles of aggregation of (a) 15 µM, (b) 20 µM, (c) 25 µM, (d) 30 µM and (e) 35 µM solutions of ***S*-G** in 15% $CHCl_3$ in IPA and corresponding fit for primary nucleation-elongation model. Here α @ 650 nm represents the degree of supramolecular polymerization monitored at 650 nm.

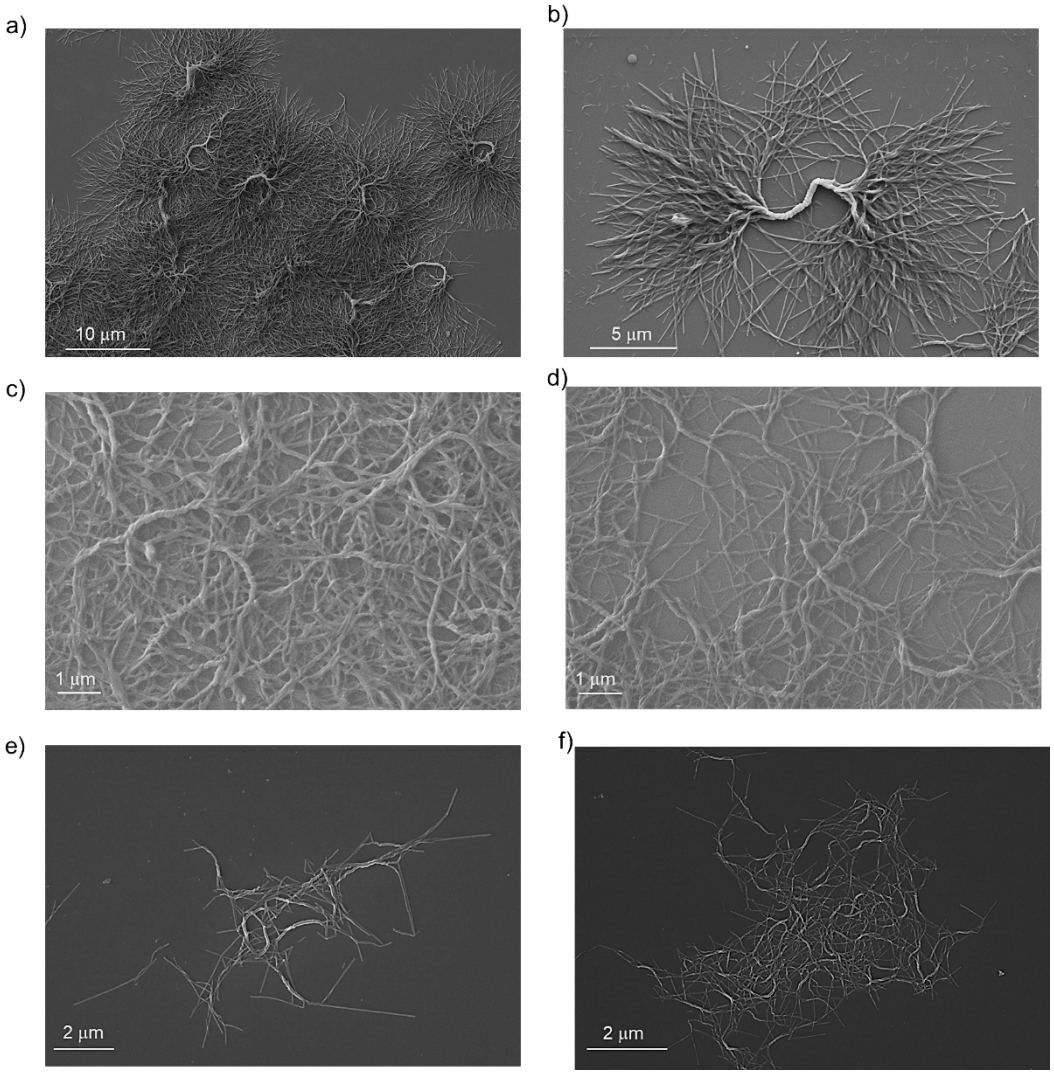

Supplementary Figure 31. Probing effect of solvent composition on morphology using FE-SEM. FE-SEM images of 30 µM solution of ***S*-G** a) and b) in 85% IPA (15% $CHCl_3$), c) and d) in 90% IPA (10% $CHCl_3$), and e) and f) in 95% IPA (5% $CHCl_3$).

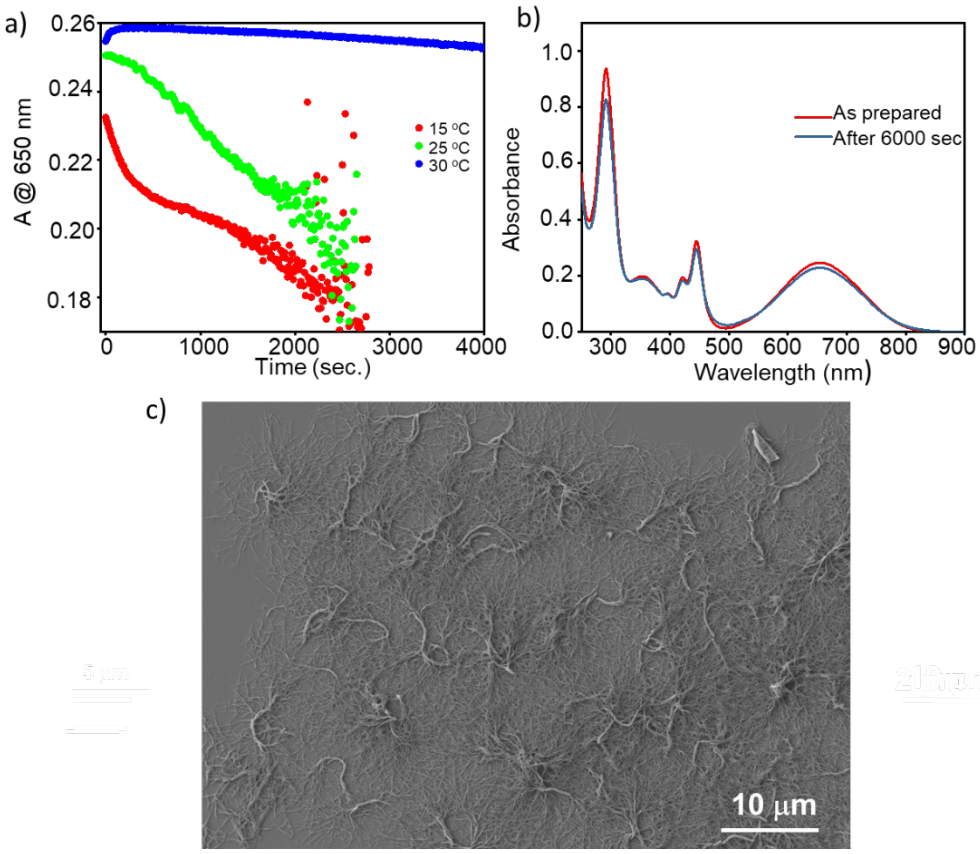

Supplementary Figure 32. Effect of temperature on the kinetics of self-assembly of *S*-G. (a) Influence of temperature on the aggregation kinetics of a 30 μM solution of ***S*-G** in 15% $CHCl_3$ in IPA at temperatures of 15 °C, 25 °C and 30 °C. (b) Comparison of absorption spectra of freshly prepared solution of ***S*-G** and after 6000 seconds, when kept at 30 °C. (c) FE-SEM image of a 30 μM solution of ***S*-G** in 15% $CHCl_3$ in IPA at 15 °C, spin-coated on silicon wafer.

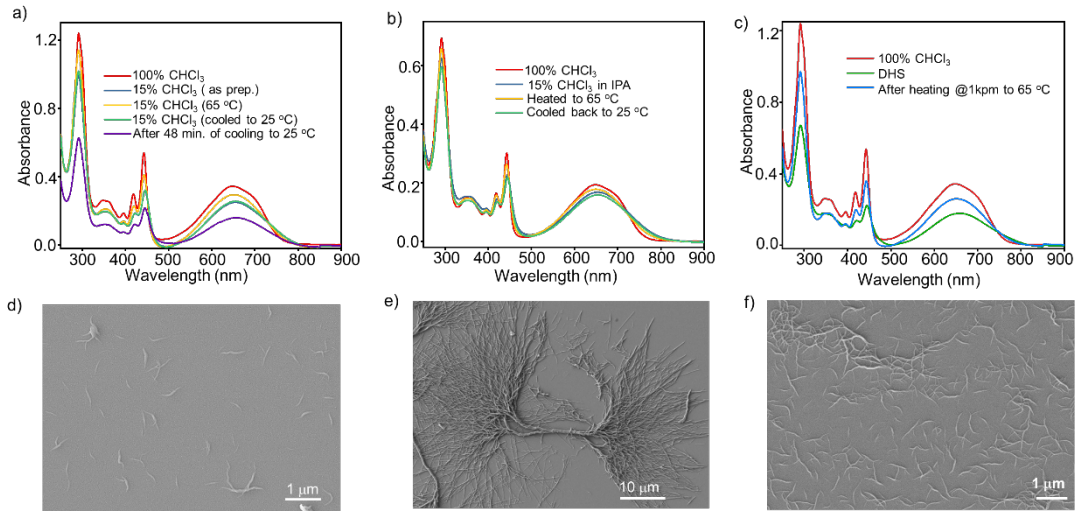

Supplementary Figure 33. Effect of temperature on the formation of DHS. (a) Effect of temperature on the absorption spectra of ***S*-G**. Heating of an as prepared solution of 30 µM in 15% $CHCl_3$ in IPA at 65 °C and its comparison with monomer (100% $CHCl_3$). After cooling back to 25 °C, the spectrum is similar to as prepared solution (15% $CHCl_3$ in IPA). (b) Effect of temperature on the absorption spectra of 15 µM solution of ***S*-G** in 15% $CHCl_3$ in IPA at 65 °C and its comparison with monomer (100% $CHCl_3$). (c) Absorption spectra of DHS of ***S*-G** and its comparison with 100 % $CHCl_3$. Upon heating, this solution does not go back to the monomeric state. FE-SEM images of a 30 µM solution of ***S*-G** in 15% $CHCl_3$ in IPA (d) heated up to 65 °C and spin-coated on silicon wafer and (e) DHS formed after it was cooled back to 25 °C and waited for 48 min. and spin-coated on silicon wafer. (f) FE-SEM image obtained by spin-coating the hot solution of DHS solution, which was heated to 65 °C.

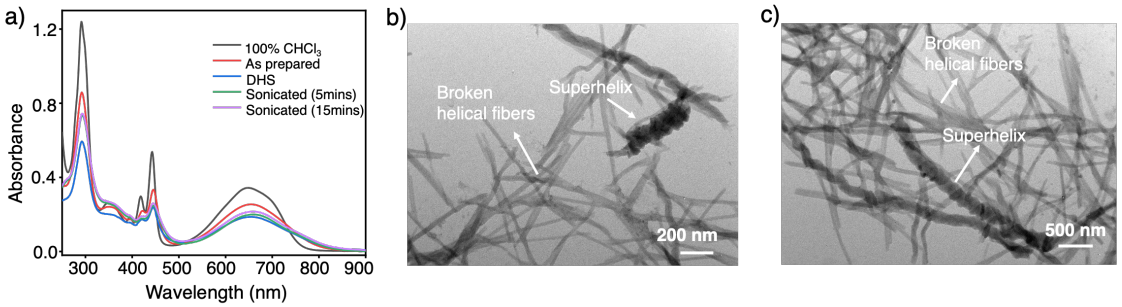

Supplementary Figure 34. Effect of sonication on the stability of DHS. (a) Effect of sonication on the absorption spectrum of DHS of a 30 μM solution of ***S*-G** in 15% $CHCl_3$ in IPA. Sonication for 5 min. and 15 min. increased the absorbance, but it does not resemble the monomeric state in pure $CHCl_3$. (b) and (c) TEM images of morphology after sonication for 15 min. shows the fragments of DHS such as super helix and thin helical fiber.

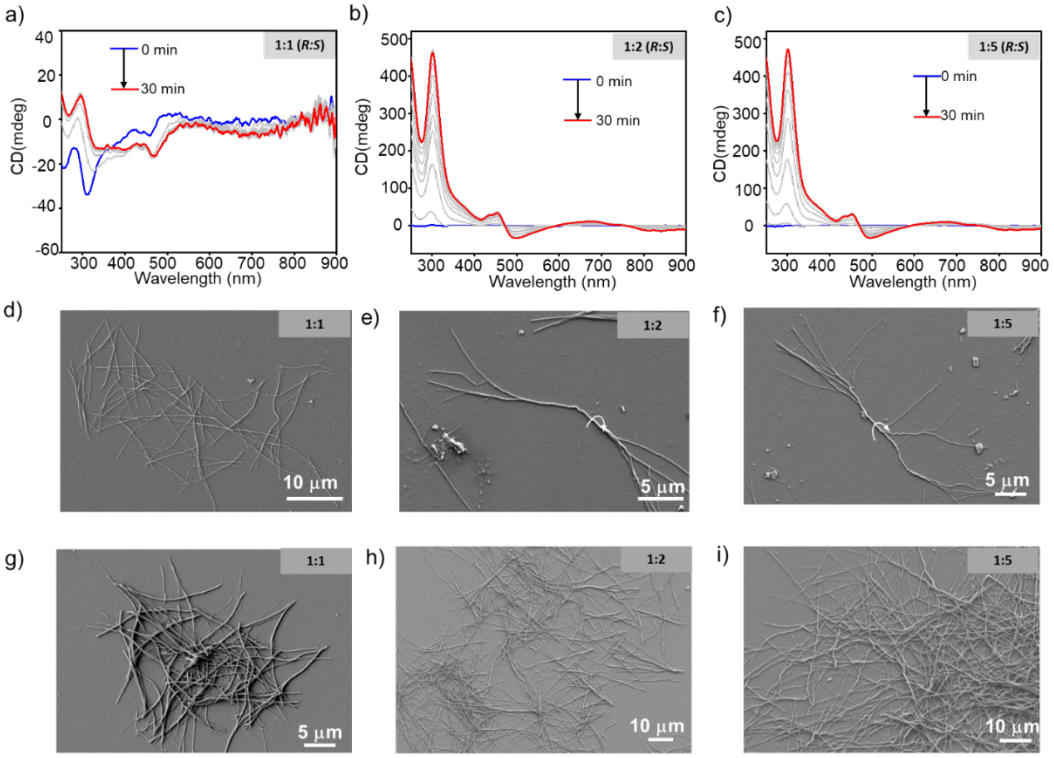

Supplementary Figure 35. Co-assembly of different ratios of *S*-G and *R*-G. Time dependant CD spectra of (a) 1:1, (b) 1:2 and (c) 1:5 mixtures of ***R*-G** and ***S*-G**. (d) and (g) FE-SEM images of 1:1 mixture of ***S*-G** and ***R*-G** spin-coated on a silicon wafer. (e) and (h) FE-SEM images of 1:2 mixture of ***S*-G** and ***R*-G** spin-coated on a silicon wafer. (f) and (i) FE-SEM images of 1:5 mixture of ***R*-G** and ***S*-G** spin-coated on a silicon wafer.

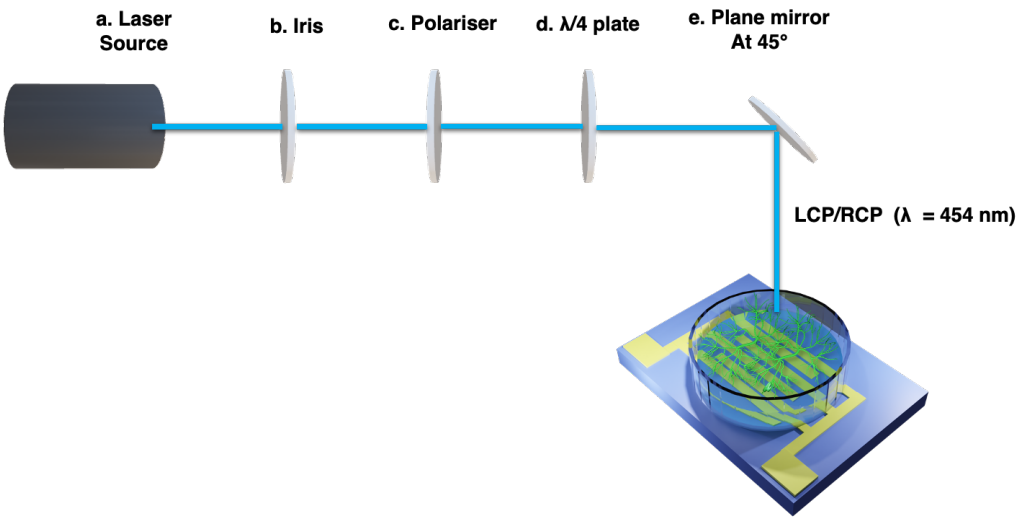

Supplementary Figure 36. Schematic of the chiro-optical measurement set up. (a) Super-continuum Laser source. (b) Iris, (c) achromatic polariser, (d) quarter-wave plate and (e) plane mirror. Optical components are procured from Thor Labs.

We performed detailed I-V measurements in solution phase for both ***S*-G** and ***R*-G** solutions and monitored the temporal evolution of the channel current which can be directly correlated with the self-assembly dynamics. Interestingly, we observe an enhancement in channel current by at least two to three times upon transition from pristine chiral monomers to DHS which can be correlated with the enhanced orderliness of the self-assembled superstructures.

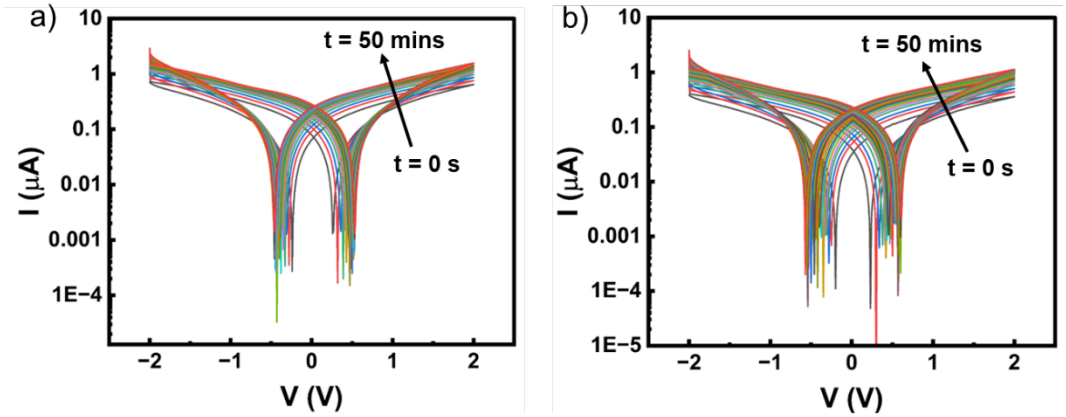

Supplementary Figure 37. Time dependant I-V measurements in solution. I-V plot measured in solution phase of (a) ***S*-G** and (b) ***R*-G** measured from t = 0 sec to t = 50 min. Note that t = 0 sec corresponds to pristine solution and 50 min. correspond to the completely self-assembled DHS.

The channel current exhibits an enhancement upon self-assembly from chiral monomers to DHS (dendritic homochiral superstructures). This follows a typical exponential growth (Supplementary Figure 38a). Upon formation of DHS, the devices exhibit preferential photoresponse towards right circularly polarized light (Supplementary Figure 38b) of wavelength 454 nm with a g-factor value reaching as high as 0.61 (inset Supplementary Figure 38b). Correspondingly, photoresponsivity as high as 2.2 mA/W was obtained.

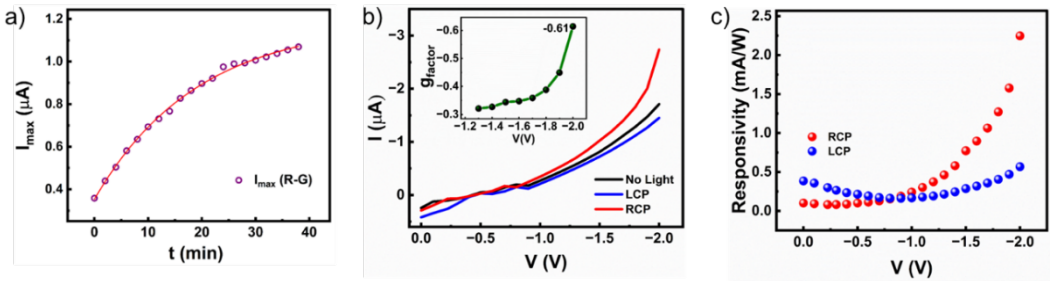

Supplementary Figure 38. Chiroptical response of dendritic homochiral superstructures (DHS) in solution. (a) Evolution of I_{max} (channel current at V = 2 V) with time (b**)** Photocurrent generated by ***R*-G** upon exposure to LCP and RCP light of λ = 454 nm. (c) Comparison of chiro-optical responsivity of ***R*-G** solution to LCP and RCP.

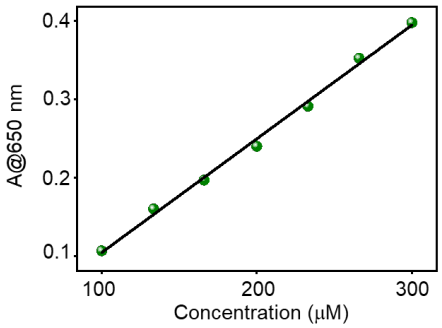

Supplementary Figure 39. Absorbance at 650 nm versus concentration of *S*-G. A plot of absorbance at 650 nm versus the concentration of ***S*-G** in $CHCl_3$, (concentrations ranging from 100 μM to 300 μM) shows a linear dependence indicating the absence of aggregates in $CHCl_3$. These are the concentrations formed when the stock solution is diluted by adding $CHCl_3$ before the addition of IPA to prepare DHS.

3. Supplementary tables

The mean square errors obtained for Secondary nucleation dominated, unseeded and primary nucleation are compared-

Supplementary Table 1. Comparison of MSE of Secondary nucleation dominated unseeded versus primary nucleation in aggregation kinetics of ***S*-G.**

Concentration	MSE (Secondary nucleation dominated, unseeded)	MSE (primary nucleation)
15 μM	0.0009308	0.01592
20 μM	0.00161	0.007131
25 μM	0.001430	0.0022672
30 μM	0.0006945	0.00116
35 μM	0.0004	0.00166

4. Supplementary references

1. Utkarsh et al. Chiral supramolecular polymer functionalized two-dimensional transition metal-based catalyst for enhancing the electrochemical water splitting via spin-polarized charge transfer. *J. Mater. Chem. A.* **2024,** 12, 20354-20363.
2. Kotha, S. et al. Cooperative Supramolecular Polymerization Guided by Dispersive Interactions. *Chem. Asian J.* **2022,** *17*, e202200494.
3. Choi, M. & Do, J. Y. Synthesis of Perylene Dianhydride-Incorporated Main Chain Polyimides and Sequential Structural Transformation through a Dipolar Cycloaddition. *React. Funct. Polym*. **2014**, *84***,** 37–44.
4. Meisl, G. et al. Molecular mechanisms of protein aggregation from global fitting of kinetic models. *Nat Prot.* **2016**, *11***,** 252-272.
5. Bannwarth, C., Ehlert, S. & Grimme, S. GFN2-xTB-an accurate and broadly parametrized self-consistent tight-binding quantum chemical method with multipole electrostatics and density-dependent dispersion contributions. *J. Chem. Theory Comput.* **2019**, *15*, 1652–1671.
6. Shao, Y. et al. Advances in molecular quantum chemistry contained in the Q-Chem 4 program package. *Mol. Phys.* **2015**, *113*, 184–215.
7. Horn, P. R., Mao, Y. & Head-Gordon, M. Probing non-covalent interactions with a second generation energy decomposition analysis using absolutely localized molecular orbitals. *Phys. Chem. Chem. Phys.* **2016**, *18*, 23067–23079.
8. Horn, P. R., Mao, Y. & Head-Gordon, M. Defining the contributions of permanent electrostatics, Pauli repulsion, and dispersion in density functional theory calculations of intermolecular interaction energies. *J. Chem. Phys.* **2016**, *144*, 114107.
9. Abraham, M. J. et al. GROMACS: High performance molecular simulations through multi-level parallelism from laptops to supercomputers. *SoftwareX* **2015**, 1–2, 19–25.
10. Van Der Spoel, D. et al. GROMACS: fast, flexible, and free. *J. Comput. Chem.* **2005**, *26*, 1701–1718.
11. Hornak, V. et al. Comparison of multiple Amber force fields and development of improved protein backbone parameters. *Proteins* **2006**, *65*, 712–725.
12. Pérez, A. et al. Refinement of the AMBER force field for nucleic acids: improving the description of alpha/gamma conformers. *Biophys. J.* **2007**, *92*, 3817–3829.
13. Case, D. A. et al. AmberTools. *J. Chem. Inf. Model.* **2023**, *63*, 6183–6191.
14. Sousa da Silva, A. W. & Vranken, W. F. ACPYPE - AnteChamber PYthon Parser interfacE. *BMC Res. Notes* **2012**, *5*, 367.
15. Bussi, G., Donadio, D. & Parrinello, M. Canonical sampling through velocity rescaling. *J. Chem. Phys.* **2007**, *126*, 014101.
16. Berendsen, H. J. C., Postma, J. P. M., van Gunsteren, W. F., DiNola, A. & Haak, J. R. Molecular dynamics with coupling to an external bath. *J. Chem. Phys.* **1984**, *81*, 3684–3690.
17. Hockney, R. W., Goel, S. P. & Eastwood, J. W. Quiet high-resolution computer models of a plasma. *J. Comput. Phys.* **1974**, *14*, 148–158.
18. Darden, T., York, D. & Pedersen, L. Particle mesh Ewald: An N·log(N) method for Ewald sums in large systems. *J. Chem. Phys.* **1993**, *98*, 10089–10092.
19. Hess, B., Bekker, H., Berendsen, H. J. C. & Fraaije, J. G. E. M. LINCS: A linear constraint solver for molecular simulations. *J. Comput. Chem.* **1997**, *18*, 1463–1472.
20. Humphrey, W., Dalke, A. & Schulten, K. VMD: visual molecular dynamics. *J. Mol. Graph.* **1996**, *14*, 33–8, 27–8.
21. Hunter, J. D. Matplotlib: A 2D Graphics Environment. *Comput. Sci. Eng.* **2007**, *9*, 90–95.

22. Waskom, M. seaborn: statistical data visualization. *J. Open Source Softw*. **2021**, *6*, 3021.

23. Sahu, R., Yamijala, S. S. R. K. C., Rao, K. V. & Reddy, S. K. Dispersion-driven cooperativity in alkyl perylene diimide oligomers: Insights from density functional theory. *Chemphyschem* **25**, e202400235 (2024).

24. Kotha, S. et al. Pathway selection in temporal evolution of supramolecular polymers of ionic π-systems: Amphiphilic organic solvent dictates the fate of water. *Chem. Eur. J.* **30**, e202303813 (2024).